COMMUNICATIONS IN COMPUTATIONAL PHYSICS
Vol. **2**, No. 4, pp. 611-639

Commun. Comput. Phys.
August 2007

Modeling of the Frozen Mode Phenomenon and its Sensitivity Using Discontinuous Galerkin Methods

S. Chun and J. S. Hesthaven*

Division of Applied Mathematics, Brown University, Providence, RI 02912, USA.

Received 19 September 2006; Accepted (in revised version) 28 November 2006
Communicated by Wei Cai
Available online 8 January 2007

Abstract. We investigate the behavior and sensitivity of the frozen mode phenomenon in finite structures with anisotropic materials, including both magnetic materials and non-normal incidence. The studies are done by using a high-order accurate discontinuous Galerkin method for solving Maxwells equations in the time domain. We confirm the existence of the phenomenon also in the time-domain and study carefully the impact of the finite crystal on the frozen mode. This sets the stage for a thorough study of the robustness of the frozen mode phenomenon, resulting in guidelines for which design parameters are most sensitive and acceptable tolerances.

AMS subject classifications: 65M60, 78A48, 78M10, 93M25

Key words: Discontinuous Galerkin method, Maxwell equation, photonic crystals, frozen mode.

1 Introduction

The use of complex metamaterials for controlling the propagation and manipulation of electromagnetic energy continues to attract significant interest among engineers. Recently, there has been a flurry of activity in the study and development of periodic structures comprising of several different anisotropic materials after it was shown that such structures could support highly unusual electromagnetic phenomena [18–20] such as a non-reciprocal propagation, very low transmission loss into the crystal and perhaps a most interesting phenomenon known as the frozen mode.

The frozen mode is a distinctive phenomenon related to stationary inflection points of the dispersion relations $\omega(k)$ such as,

$$\frac{\partial\omega}{\partial k}=0;\quad \frac{\partial^2\omega}{\partial k^2}=0;\quad \frac{\partial^3\omega}{\partial k^3}\neq 0\quad \text{at } \omega=\omega_0.$$

*Corresponding author. *Email addresses:* schun@dam.brown.edu (S. Chun), Jan.Hesthaven@Brown.edu (J. S. Hesthaven)

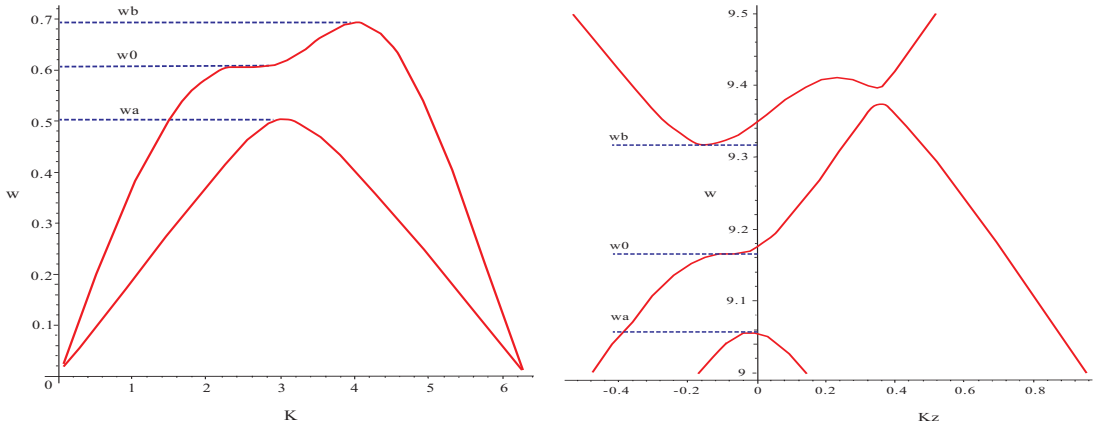

Figure 1: Dispersion relations for two different types of layer. Left: gyrotropic photonic crystals ($\omega_b = 0.690320778$, $\omega_0 = 0.607676756$, $\omega_a = 0.502044368$) and right: oblique anisotropic layers ($\omega_b = 9.3160209805$, $\omega_0 = 9.164450223$, $\omega_a = 9.0569705995$). ω and k are expressed in units of c/L and 1/L.

When a monochromatic wave with frequency ω_0 propagates into a periodic array of unit cells with this dispersion relation, the wave shows the following striking features due to the significantly large transmittance rate at inflection points contrary to the negligible transmittance rate at band edges [18],

- dramatic slow-down of the waves
- enormously increased field amplitude
- cup-like singularity of the transmittance rate
- unidirectionality of monochromatic waves.

Let us briefly explain these features in the following. Fig. 1 shows two different types of dispersion relation for two different layers, but both of them contain the same kind of inflection point ω_0. At each ω_0 in Fig. 1, we have two eigenmodes k_0 and k_1 such that $\frac{\partial\omega}{\partial k}|_{k=k_0} = 0$, $\frac{\partial\omega}{\partial k}|_{k=k_1} < 0$ and only the eigenmode at k_1 transfers the energy. Since we have no eigenmode with a positive group velocity, the transmitted wave does not transfer the energy in the direction of the propagation. Physically, it means that the incident electromagnetic wave slows down with infinitesimal group velocity within the periodic layers. However, if a wave propagates in the opposite direction, we have $\frac{\partial\omega}{\partial k}|_{k=k_1} > 0$ and the eigenmode k_1 transfers the energy and consequently the abnormal slow-down vanishes. Thus, the crystal behaves differently depending on the vector of propagation, a phenomenon known as *electromagnetic unidirectionality*.

When the frequency of the wave is close to ω_0, a transmitted wave consists of propagation components and evanescent components. The latter decays as the wave proceeds along the propagation direction, but the former remains to propagate. Both components initially increase dramatically, but their magnitudes remain almost equal with opposite sign. Thus, the field amplitude at the interface of the layer and vacuum remain almost the same, but once the wave precedes into the slab, the evanescent components die out

and only the dramatically amplified propagation components remain and contribute to the increase of the field amplitude. This propagation of amplified extended mode also explains the abnormal cup-like singularity of transmittance coefficients depending on the incident wave polarization.

These unique features of the frozen mode have been attractive for numerous practical applications, but the existence of frozen mode itself was theoretically based on at least two impractical assumptions: *infinity* and *periodicity*. Furthermore, all parameters for the above dispersion relations should be exact up to at least $3 \sim 4$ digits with an infinite number of unit cells stacked up along z direction to yield the desired phenomena.

However, in real applications a layer cannot be infinitely long and every unit cell cannot be exactly the same due to practical limitations in the fabrication. These issues could prohibit the realization of frozen mode, although Figotin and Vitebsky suggested in [19] that the phenomena would be robust, since the density of modes of inflection points is abnormally stronger than that of band edges.

Hence, it is natural to study the impact of finiteness of the crystals as well as the sensitivity of the phenomenon to variations in some of the parameters, e.g., material parameters, degree of anisotropy etc, to gain an improved understanding of the practicality of utilizing the frozen mode phenomena.

For this investigation, we use a discontinuous Galerkin method (DG) with a multi-element formulation for the modeling of the frozen mode in the time domain [1, 2]. We have adopted the scattered formulation for Maxwell equation to ease the boundary conditions concerning scattered objects and we put Absorbing boundary condition (ABC) at the end of the z-direction to prevent unnecessary reflected waves.

The remaining part of the paper is organized as follows. In Section 2, we briefly discuss Maxwell's equations in the time domain. In Section 3, the details of the schemes including discontinuous Galerkin Methods, time stepping, filtering and absorbing boundary condition are described and also several numerical tests with their results are shown. Section 4 discusses the modeling of the frozen mode with a large number of unit cells and assess the effect of a finite number of unit cells. In Section 5, we study the sensitivity of the frozen mode phenomena to variations in critical parameters while concluding remarks are given in Section 6.

2 Formulation

We model two different types of layers. The one array is referred to as a gyrotropic photonic crystal and it consists of two anisotropic materials with different in-plane misalignments $(\mathbf{A_1}, \mathbf{A_2})$ and one strong magnetic material ($\mathbf{F}$) (see the left of Fig. 2). When it is in a certain special combination, it shows the strong Faraday rotation (circular birefringence) of light polarization in the absence of magnetic field, which results in spectral nonreciprocity $(\omega(\vec{k}) \neq \omega(-\vec{k}))$ [11–13, 18, 19].

The other configuration is a nonmagnetic periodic stack with oblique anisotropy di-

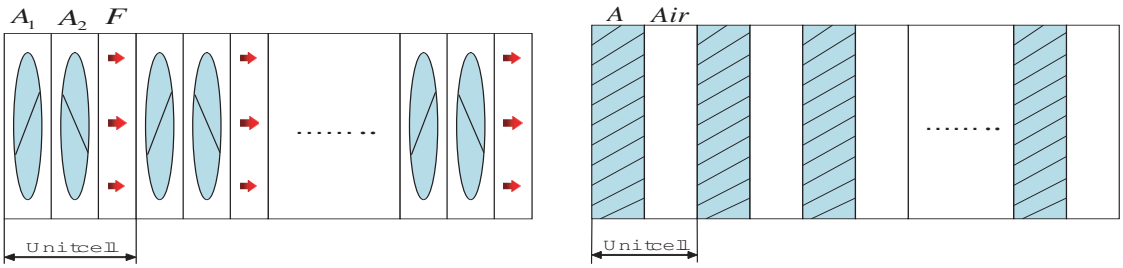

Figure 2: Periodic structure of gyrotropic photonic crystals consisting of two different anisotropic materials with one magnetic layer (left) and oblique anisotropic layers consisting of one anisotropic material with vacuum (right). **A**: anisotropic layer, **F**: magnetic layer, **Air**: air-filled gap.

electric materials with ($\varepsilon_{xy} \neq 0$) and air-filled gap between them [12, 13, 21] (see the right of Fig. 2). If an incident wave is propagating into the layer at an oblique angle, then the axial spectral asymmetry is obtained, i.e., $\omega(\vec{k}_x,\vec{k}_y,\vec{k}_z) \neq \omega(\vec{k}_x,\vec{k}_y,-\vec{k}_z)$.

In the remaining part of this section, we describe the discrete formulations of Maxwell's equations for these two different layers. For simplicity, we call the former case as the magnetic frozen mode and the latter as the oblique frozen mode.

2.1 The magnetic frozen mode

We consider the following Maxwell's equations

$$\nabla \times \tilde{\mathbf{E}} = -\frac{d\tilde{\mathbf{B}}}{dt}, \quad \nabla \times \tilde{\mathbf{H}} = \frac{d\tilde{\mathbf{D}}}{dt},$$

where $\tilde{\mathbf{E}}$ and $\tilde{\mathbf{H}}$ are the electric field and the magnetic field, respectively while $\tilde{\mathbf{D}}$ and $\tilde{\mathbf{B}}$ the displacement field and the induction field. If the direction of the wave propagation z is normal to the layers, these fields are related by linear constitutive relations as follows.

$$\tilde{\mathbf{D}}(z) = \hat{\varepsilon}(z)\tilde{\mathbf{E}}(z), \quad \tilde{\mathbf{B}}(z) = \hat{\mu}(z)\tilde{\mathbf{H}}(z),$$

where, hat indicates the corresponding quantity is a matrix. These relations yield the following Maxwell's equations in the time domain.

$$\nabla \times \tilde{\mathbf{E}} = -\hat{\mu}^r(z)\frac{\partial \tilde{\mathbf{H}}}{\partial t} - \omega\hat{\mu}^i(z)\tilde{\mathbf{H}}, \quad \nabla \times \tilde{\mathbf{H}} = \hat{\varepsilon}^r(z)\frac{\partial \tilde{\mathbf{E}}}{\partial t} + \omega\hat{\varepsilon}^i(z)\tilde{\mathbf{E}}. \tag{2.1}$$

The superscript r,i denotes the real part and the imaginary part of the components, respectively and ω is the center frequency for which these material parameters are given. To simplify the above equations, we introduce the normalized quantities using

$$z = \frac{\tilde{z}}{\tilde{L}}, \quad t = \frac{\tilde{t}}{\tilde{L}/\tilde{c}_0},$$

where, $\tilde{L}$ is a reference length and $\tilde{c_0}=(\tilde{\varepsilon}_0\tilde{\mu}_0)^{\frac{1}{2}}$ is the dimensional speed of light in vacuum when $\tilde{\varepsilon_0}$ and $\tilde{\mu_0}$ refer to the vacuum permittivity and permeability respectively. Also, $\tilde{\mathbf{E}}$ and $\tilde{\mathbf{H}}$ are normalized as

$$\mathbf{E}=\sqrt{\frac{\tilde{\varepsilon_0}}{\tilde{\mu_0}}}\frac{\tilde{\mathbf{E}}}{\tilde{H}_0},\qquad \mathbf{H}=\frac{\tilde{\mathbf{H}}}{\tilde{H}_0},$$

where $\tilde{H}_0$ is a dimensional reference magnetic field strength. By substituting these normalized quantities into Eq. (2.1), we obtain the following non-dimensionalized equations

$$\nabla\times\mathbf{E}=-\hat{\mu}^r(z)\frac{\partial\mathbf{H}}{\partial t}-2\pi\hat{\mu}^i(z)\mathbf{H},\qquad \nabla\times\mathbf{H}=\hat{\varepsilon}^r(z)\frac{\partial\mathbf{E}}{\partial t}+2\pi\hat{\varepsilon}^i(z)\mathbf{E}, \tag{2.2}$$

which is the most general model for what we shall consider. For the magnetic frozen mode, we consider the following material constant of $\hat{\varepsilon}$, $\hat{\mu}$.

$$\hat{\varepsilon}=\hat{\varepsilon}^r+i\hat{\varepsilon}^i,\quad \hat{\varepsilon}^r=\begin{bmatrix}\varepsilon_{xx} & \varepsilon^r_{xy}\\ \varepsilon^r_{xy} & \varepsilon_{yy}\end{bmatrix},\quad \hat{\varepsilon}^i=\begin{bmatrix}0 & \varepsilon^i_{xy}\\ -\varepsilon^i_{xy} & 0\end{bmatrix},$$
$$\hat{\mu}=\hat{\mu}^r+i\hat{\mu}^i,\quad \hat{\mu}^r=\begin{bmatrix}\mu_{xx} & \mu^r_{xy}\\ \mu^r_{xy} & \mu_{yy}\end{bmatrix},\quad \hat{\mu}^i=\begin{bmatrix}0 & \mu^i_{xy}\\ -\mu^i_{xy} & 0\end{bmatrix}.$$

Then, we obtain the explicit Maxwell's equations for the modeling of the magnetic frozen mode on the form

$$\begin{aligned}
&\varepsilon_{xx}\frac{\partial E_x}{\partial t}+\varepsilon^r_{xy}\frac{\partial E_y}{\partial t}=-\frac{\partial H_y}{\partial z}-2\pi\varepsilon^i_{xy}E_y,\\
&\varepsilon^r_{xy}\frac{\partial E_x}{\partial t}+\varepsilon_{yy}\frac{\partial E_y}{\partial t}=\frac{\partial H_x}{\partial z}+2\pi\varepsilon^i_{xy}E_x,\\
&\mu_{xx}\frac{\partial H_x}{\partial t}+\mu^r_{xy}\frac{\partial H_y}{\partial t}=\frac{\partial E_y}{\partial z}-2\pi\mu^i_{xy}H_y,\\
&\mu^r_{xy}\frac{\partial H_x}{\partial t}+\mu_{yy}\frac{\partial H_y}{\partial t}=-\frac{\partial E_x}{\partial z}+2\pi\mu^i_{xy}H_x.
\end{aligned}$$

Note that ε^i_{xy} and μ^i_{xy} are not loss, but responsible for the Faraday rotation of the electromagnetic waves. Thus, the above equations preserve energy and can be easily shown to be stable in the sense that $\frac{d\mathbf{E}^\Omega}{dt}=0$ when the energy $\mathbf{E}^\Omega$ is defined as $\mathbf{E}^\Omega=\int_\Omega \vec{E}^T\hat{\varepsilon}\vec{E}+\vec{H}^T\hat{\mu}\vec{H}$.

When the materials are given as follows [19], we recover the dispersion relation as shown in Fig. 1 (left).

$$\text{For } \mathbf{A} \text{ layer}:\quad \hat{\varepsilon}=\begin{bmatrix}13.61+12.40\cos(2\phi) & 12.40\sin(2\phi)\\ 12.40\sin(2\phi) & 13.61-12.40\cos(2\phi)\end{bmatrix},\quad \hat{\mu}=\begin{bmatrix}1 & 0\\ 0 & 1\end{bmatrix};$$
$$\text{For } \mathbf{F} \text{ layer}:\quad \hat{\varepsilon}=\begin{bmatrix}5.0 & 0.0\\ 0.0 & 5.0\end{bmatrix},\quad \hat{\mu}=\begin{bmatrix}60.0 & i37.0\\ -i37.0 & 60.0\end{bmatrix},$$

where, ϕ is the misalignment angle of the two anisotropic layers and we let $\phi_1 = 0$ for the first anisotropic layer and $\phi_2 = \pi/4$ for the second anisotropic layer. Also, we take the thickness of the F layer as 0.0047454 (L) and the frequency of incident wave $\omega =$ 0.607676756 (c/L), where L is the thickness of unit cell and c is the speed of light in vacuum.

2.2 The oblique frozen mode

The structure of this crystal seems to be much simpler than the gyrotropic photonic crystal, but in order to achieve the axial spectral asymmetry ($\omega(\vec{k}_x,\vec{k}_y,\vec{k}_z) \neq \omega(\vec{k}_x,\vec{k}_y,-\vec{k}_z)$), the following two conditions should be satisfied: the oblique anisotropy should not be in-plane or axial and the Bloch wave $\vec{k}$ has to be oblique to the layers, i.e.,

$$1)\ \varepsilon_{xz} \neq 0 \ \text{ and/or } \ \varepsilon_{yz} \neq 0, \qquad 2)\ k_x \neq 0 \ \text{ and/or } \ k_y \neq 0.$$

Assume that their tangential components k_x,k_y are all the same for the incident, reflected, and transmitted waves and let only k_z be different. In other words, we seek a solution of the following form

$$\mathbf{E}(x,y,z) = e^{i(k_x x + k_y y)} E(z), \quad \mathbf{H}(x,y,z) = e^{i(k_x x + k_y y)} H(z).$$

When this form of the solution is substituted, we have six equations, but considering only k_z components, the last row of each equation in Eq. (2.1) can be used to complement the other equations. Thus, similar to the magnetic frozen mode, we have only four equations. The explicit equations for the oblique frozen mode modeling are expressed as

$$\begin{aligned}
&n_x \frac{\varepsilon_{xz}}{\varepsilon_{zz}} \frac{\partial E_x}{\partial t} - n_x n_y \frac{1}{\varepsilon_{zz}} \frac{\partial H_x}{\partial t} + \left(n_x^2 \frac{1}{\varepsilon_{zz}} - 1 \right) \frac{\partial H_y}{\partial t} = \frac{\partial E_x}{\partial z}, \\
&n_y \frac{\varepsilon_{xz}}{\varepsilon_{zz}} \frac{\partial E_x}{\partial t} + \left(1 - n_y^2 \frac{1}{\varepsilon_{zz}} \right) \frac{\partial H_x}{\partial t} + n_x n_y \frac{1}{\varepsilon_{zz}} \frac{\partial H_y}{\partial t} = \frac{\partial E_y}{\partial z}, \\
&n_y^2 \frac{\partial E_x}{\partial t} + (\varepsilon_{yy} - n_x^2) \frac{\partial E_y}{\partial t} = \frac{\partial H_x}{\partial t}, \\
&\left(n_y^2 - \varepsilon_{xx} + \frac{\varepsilon_{xz}^2}{\varepsilon_{zz}} \right) \frac{\partial E_x}{\partial t} - n_x n_y \frac{\partial E_y}{\partial t} - n_x \frac{\varepsilon_{xz}}{\varepsilon_{zz}} \frac{\partial H_x}{\partial t} + n_y \frac{\varepsilon_{xz}}{\varepsilon_{zz}} \frac{\partial H_y}{\partial t} = \frac{\partial H_y}{\partial z},
\end{aligned}$$

where $n_x = ck_x/\omega$, $n_y = ck_y/\omega$.

With the following materials specified as in [21], we obtain the dispersion relation as shown in Fig. 1 (right).

$$\hat{\varepsilon}_A = \begin{bmatrix} 4.62\cos\theta^2 + 3.78\sin\theta^2 & 0 & 0.84\cos\theta\sin\theta \\ 0 & 4.62 & 0 \\ 0.84\cos\theta\sin\theta & 0 & 3.78\cos\theta^2 + 4.62\sin\theta^2 \end{bmatrix}_{\theta=\pi/4},$$

$$\hat{\varepsilon}_B = \begin{bmatrix} 1 & 0 & 0 \\ 0 & 1 & 0 \\ 0 & 0 & 1 \end{bmatrix}, \quad \hat{\mu}_A = \hat{\mu}_B = I.$$

We let the thickness of A layer be the same as that of vacuum. Also, the tangential components of the incident wave vector are $n_x = n_y = -0.493489$ and the frequency of the wave is 9.164450223 (c/L).

3 Numerical scheme

Let $\mathbf{q} = [E_x\ E_y\ H_x\ H_y]$. Then, the two equations with different material coefficients are reduced to the general problem of the form

$$\frac{\partial \mathbf{q}}{\partial t} + \frac{\partial \mathbf{q}}{\partial z}\hat{\mathbf{A}} + \mathbf{q}\hat{\mathbf{B}} = \mathbf{0}. \tag{3.1}$$

For the magnetic frozen mode,

$$\begin{aligned}
&\hat{\mathbf{A}} = \mathbf{A}\mathbf{Q}^{-1}, \quad \hat{\mathbf{B}} = \mathbf{B}\mathbf{Q}^{-1},\\
&\mathbf{Q} = \begin{bmatrix} \mathbf{Q}_{11} & \mathbf{0} \\ \mathbf{0} & \mathbf{Q}_{22} \end{bmatrix}, \quad \mathbf{Q}_{11} = \begin{bmatrix} \varepsilon_{xx} & \varepsilon^r_{xy} \\ \varepsilon^r_{xy} & \varepsilon_{yy} \end{bmatrix}, \quad \mathbf{Q}_{22} = \begin{bmatrix} \mu_{xx} & \mu^r_{xy} \\ \mu^r_{xy} & \mu_{yy} \end{bmatrix},\\
&\mathbf{A} = \begin{bmatrix} \mathbf{0} & \mathbf{A}_{12} \\ \mathbf{A}_{21} & \mathbf{0} \end{bmatrix}, \quad \mathbf{A}_{12} = \begin{bmatrix} 0 & -1 \\ 1 & 0 \end{bmatrix}, \quad \mathbf{A}_{21} = \begin{bmatrix} 0 & 1 \\ -1 & 0 \end{bmatrix},\\
&\mathbf{B} = \begin{bmatrix} \mathbf{B}_{11} & \mathbf{0} \\ \mathbf{0} & \mathbf{B}_{22} \end{bmatrix}, \quad \mathbf{B}_{11} = \begin{bmatrix} 0 & -\varepsilon^i_{xy} \\ \varepsilon^i_{xy} & 0 \end{bmatrix}, \quad \mathbf{B}_{22} = \begin{bmatrix} 0 & -\mu^i_{xy} \\ \mu^i_{xy} & 0 \end{bmatrix},
\end{aligned}$$

and for the oblique frozen mode,

$$\begin{aligned}
&\hat{\mathbf{A}} = \mathbf{Q}^{-1}, \quad \hat{\mathbf{B}} = \mathbf{0},\\
&\mathbf{Q} = \begin{bmatrix} \mathbf{Q}_{11} & \mathbf{Q}_{12} \\ \mathbf{Q}_{21} & \mathbf{Q}_{22} \end{bmatrix},\\
&\mathbf{Q}_{11} = \begin{bmatrix} n_x(\varepsilon_{xz}/\varepsilon_{zz}) & 0 \\ n_y(\varepsilon_{xz}/\varepsilon_{zz}) & 0 \end{bmatrix}, \quad \mathbf{Q}_{12} = \begin{bmatrix} -n_x n_y(1/\varepsilon_{zz}) & n_x^2(1/\varepsilon_{zz}) - 1 \\ 1 - n_y^2(1/\varepsilon_{zz}) & n_x n_y(1/\varepsilon_{zz}) \end{bmatrix},\\
&\mathbf{Q}_{21} = \begin{bmatrix} n_x n_y & \varepsilon_{yy} - n_x^2 \\ n_y^2 - \varepsilon_{xx} + \varepsilon_{xz}^2/\varepsilon_{zz} & -n_x n_y \end{bmatrix}, \quad \mathbf{Q}_{22} = \begin{bmatrix} 0 & 0 \\ -n_y(\varepsilon_{xz}/\varepsilon_{zz}) & n_x(\varepsilon_{xz}/\varepsilon_{zz}) \end{bmatrix}.
\end{aligned}$$

Suppose that the domain Ω can be segmented into K non-overlapping layers. In each elements, we assume that the approximated solution $\mathbf{q}^k_N(z,t)$ can be represented as an N'th order polynomial, i.e.,

$$\mathbf{q}^k_N(z,t) = \sum_{i=0}^{N} \hat{\mathbf{q}}^k_i \phi_i(z^k) = \sum_{i=0}^{N} \mathbf{q}^k_i(t)\ell^k_i(z^k), \tag{3.2}$$

where, z^k is in the element $[z^k_-, z^k_+]$ which is linearly mapped satisfying $z^k(-1)=z^k_-$, $z^k(1)=z^k_+$. Also note that ℓ^k_i is Lagrange polynomial based on grid points z^k_i. There are many

ways in choosing ϕ_n and segmentation of the domain Ω, but for easy implementation with high accuracy and efficiency, we use Legendre polynomials $P_n(z)$ [10] for $\phi(z)$. Then ϕ and ℓ_i have the following relation

$$\hat{\mathbf{V}}^T\vec{\ell}^k(z^k)=\vec{\phi}(z^k),\qquad \hat{\mathbf{V}}=[V_{ij}]=[P_j(z_i)], \tag{3.3}$$

where

$$\vec{\ell}^k=[\ell_0^k\ \ell_1^k\cdots\ell_N^k],\qquad \vec{\phi}^k=[\phi_0^k\ \phi_1^k\cdots\phi_N^k].$$

The semi-discrete scheme is derived by requiring that

$$\int_{z_-^k}^{z_+^k}\left(\frac{\partial\mathbf{q}_N}{\partial t}+\frac{\partial\mathbf{q}_N}{\partial z}\hat{\mathbf{A}}+\mathbf{q}_N\hat{\mathbf{B}}\right)\ell_i^k(z)dz=\mathbf{0},\quad 0\le i\le N.$$

Executing two integrations by parts, we have the following form,

$$\int_{z_-^k}^{z_+^k}\left(\frac{\partial\mathbf{q}_N}{\partial t}+\frac{\partial\mathbf{q}_N}{\partial z}\hat{\mathbf{A}}+\mathbf{q}_N\hat{\mathbf{B}}\right)\ell_i^k(z)dz=\int_{z_-^k}^{z_+^k}\hat{n}\left[(\mathbf{q}_N\hat{\mathbf{A}})^--(\mathbf{q}_N\hat{\mathbf{A}})^*\right]\ell_i^k(z)dz, \tag{3.4}$$

where $\hat{n}$ is an outward normal vector. Here, we use a numerical flux $(\mathbf{q}_N\hat{\mathbf{A}})^*$ such that

$$[\mathbf{q}_N\hat{\mathbf{A}}]^*=(\mathbf{q}_N^-,\mathbf{q}_N^+)\hat{\mathbf{A}},$$

where $\mathbf{q}^-$ is a local solution and $\mathbf{q}^+$ a solution in the neighboring element. The reason we need a flux in the above equation is that there are two different solutions on the same interface, since $z_+^k=z_-^{k+1}$. Among many possible fluxes, upwind flux [6] or a simpler central flux [1] are often preferred. We shall use the central flux for our semi-discrete scheme as following

$$(\mathbf{q}_N^-,\mathbf{q}_N^+)\hat{\mathbf{A}}=\frac{1}{2}(\mathbf{q}_N^++\mathbf{q}_N^-)\hat{\mathbf{A}}. \tag{3.5}$$

Let us define the following mass matrix and stiff matrix ($h^k=z_+^k-z_-^k$)

$$M_{ij}=\int_{z_-^k}^{z_+^k}\ell_i^k(z^k)\ell_j^k(z^k)dz^k=\frac{h^k}{2}\int_{-1}^{1}\ell_i(r)\ell_j(r)dr,$$
$$S_{ij}=\int_{z_-^k}^{z_+^k}\ell_i^k(z^k)\frac{d\ell_j}{dz}dz^k=\int_{-1}^{1}\ell_i(r)\frac{d\ell_j}{dr}dr,\quad 0\le i,j\le N.$$

Then, using Eq. (3.3) we obtain the following relation

$$\mathbf{M}=(\mathbf{V}^{-1})^T\mathbf{V}^{-1},\quad \mathbf{S}=(\mathbf{V}^T)^{-1}\mathbf{W}\mathbf{V}^{-1},\quad W_{ij}=\int_{-1}^{1}\phi_i(r)\phi_j'(r)dr.$$

With the definition of the above matrix and the central flux, Eq. (3.5), we have the following local semi-discrete scheme:

$$\frac{h^k}{2}\hat{\mathbf{M}}\frac{d\mathbf{q}_N}{dt}+\hat{\mathbf{S}}\mathbf{q}_N\hat{\mathbf{A}}+\frac{h^k}{2}\hat{\mathbf{M}}\mathbf{q}_N\hat{\mathbf{B}}=\frac{e_0}{2}\left[(-\mathbf{q}_N^-+\mathbf{q}_N^+)\hat{\mathbf{A}}\right]_{z_-^k}+\frac{e_N}{2}\left[(\mathbf{q}_N^--\mathbf{q}_N^+)\hat{\mathbf{A}}\right]_{z_+^k}, \tag{3.6}$$

where e_i is a N+1 long zero vector with 1 only for its i-th component and $[\ ]_a$ refers to the evaluation of $[\ ]$ at $x=a$. We see that the inverse of $\hat{\mathbf{M}}$ exists and can be easily computed because it is only a local matrix, thus by multiplying $\hat{\mathbf{M}}^{-1}$, we finally obtain our semi-discrete scheme

$$\frac{d\mathbf{q}_N}{dt}+\frac{2}{h^k}(\hat{\mathbf{M}}^{-1}\hat{\mathbf{S}})\mathbf{q}_N\hat{\mathbf{A}}+\mathbf{q}_N\hat{\mathbf{B}}=\frac{e_0}{h^k}\left[\hat{\mathbf{M}}^{-1}(-\mathbf{q}_N^-+\mathbf{q}_N^+)\hat{\mathbf{A}}\right]_{z_-^k}+\frac{e_N}{h^k}\left[\hat{\mathbf{M}}^{-1}(\mathbf{q}_N^--\mathbf{q}_N^+)\hat{\mathbf{A}}\right]_{z_+^k},$$

which reads in the scattered field formulation,

$$\begin{aligned}\frac{d\mathbf{q}_N^{scat}}{dt}=&-\frac{2}{h^k}(\hat{\mathbf{M}}^{-1}\hat{\mathbf{S}})\mathbf{q}_N^{scat}\hat{\mathbf{A}}-\mathbf{q}_N^{scat}\hat{\mathbf{B}}+(\hat{\mathbf{Q}}^{-1}-\mathbf{I})\frac{d\mathbf{q}_N^{inc}}{dt}-\mathbf{q}_N^{inc}\hat{\mathbf{B}}\\&+\frac{e_0}{h^k}\left[\hat{\mathbf{M}}^{-1}(-(\mathbf{q}_N^{scat})^-+(\mathbf{q}_N^{scat})^+)\hat{\mathbf{A}}\right]_{z_-^k}+\frac{e_N}{h^k}\left[\hat{\mathbf{M}}^{-1}((\mathbf{q}_N^{scat})^--(\mathbf{q}_N^{scat})^+)\hat{\mathbf{A}}\right]_{z_+^k},\end{aligned} \tag{3.7}$$

where $\mathbf{q}^{inc}$ represents the incident field and $\mathbf{q}^{scat}$ the scattered field. Note that for the scattered field formulation, only the scattered field is computed in the problem space and the incident field is specified analytically throughout the problem space.

The consistency of this scheme can be easily proved from the general polynomial approximation theorems. Furthermore, stability can be shown using energy methods as discussed in detail in [3].

3.1 Time stepping

For the time marching, we can use the classical 4th order Runge-Kutta scheme. However, for explicit time-integration schemes the stable time step will scale as

$$\Delta t\propto\frac{h}{N^2}$$

with N being the order of approximation and h being the length of the smallest interval. In the particular applications being considered the very thin magnetic F layers will prove that the explicit time-integration prohibitive.

To overcome the long time integration due to an excessively small time step, we use a Diagonally Implicit-Runge-Kutta (DIRK) 3rd order method [9]. The L-stability of this DIRK 3rd order method enables us to choose Δt independent of the size of the elements to the extend of acceptable accuracy. Considering the linearity of the equations, we can rewrite (3.7) as following by introducing matrices $\hat{\mathbf{T}}^s$,$\hat{\mathbf{T}}^i$,

$$\frac{d\mathbf{q}_N^{scat}}{dt}=\hat{\mathbf{T}}^s\mathbf{q}_N^{scat}(t)+\hat{\mathbf{T}}^i\mathbf{q}_N^{inc}(t).$$

Then, applying the DIRK 3rd order yields

$$\begin{aligned}
(I-\gamma\Delta t\hat{\mathbf{T}}^s)\mathbf{Y}_1^{scat} &= \mathbf{q}_N^{scat}(t)+\Delta t\ [\gamma\hat{\mathbf{T}}^i\mathbf{q}_N^{inc}(t+c_1\Delta t)],\\
(I-\gamma\Delta t\hat{\mathbf{T}}^s)\mathbf{Y}_2^{scat} &= \mathbf{q}_N^{scat}(t)+\Delta t\ [a_{21}(\hat{\mathbf{T}}^sY_1+\hat{\mathbf{T}}^i\mathbf{q}_N^{inc}(t+c_1\Delta t))+\gamma\hat{\mathbf{T}}^i\mathbf{q}_N^{inc}(t+c_2\Delta t)],\\
(I-\gamma\Delta t\hat{\mathbf{T}}^s)\mathbf{Y}_3^{scat} &= \mathbf{q}_N^{scat}(t)+\Delta t\ [a_{31}(\hat{\mathbf{T}}^sY_1+\hat{\mathbf{T}}^i\mathbf{q}_N^{inc}(t+c_1\Delta t))\\
&\quad +a_{32}(\hat{\mathbf{T}}^s\mathbf{Y}_2+\hat{\mathbf{T}}^i\mathbf{q}_N^{inc}(t+c_2\Delta t))+\gamma\hat{\mathbf{T}}^i\mathbf{q}_N^{inc}(t+c_3\Delta t)],\\
\mathbf{q}_N^{scat} &= \mathbf{q}_N^{scat}+\Delta t\ [b_1(\hat{\mathbf{T}}^s\mathbf{Y}_1+\hat{\mathbf{T}}^i\mathbf{q}_N^{inc}(t+c_1\Delta t))\\
&\quad +b_2(\hat{\mathbf{T}}^s\mathbf{Y}_2+\hat{\mathbf{T}}^i\mathbf{q}_N^{inc}(t+c_2\Delta t))+b_3(\hat{\mathbf{T}}^s\mathbf{Y}_3+\hat{\mathbf{T}}^i\mathbf{q}_N^{inc}(t+c_3\Delta t))].
\end{aligned}$$

The Butcher tableau for the considered DIRK scheme is given as

c_1	γ	0	0	0.4358665215	0.4358665215	0	0
c_2	a_{21}	γ	0	0.7179332608	0.2820667392	0.4358665215	0
c_3	a_{31}	a_{32}	γ	1	1.208496649	-0.644363171	0.4358665215
	b_1	b_2	b_3		1.208496649	-0.644363171	0.4358665215

For the 3rd order DIRK method, the most critical issue is to invert $(I-\gamma\Delta t\hat{\mathbf{T}}^s)$ efficiently. However, for the one dimensional DG method, $(I-\gamma\Delta t\hat{\mathbf{T}}^s)$ is very sparse and well distributed along the diagonal elements. Therefore, it is easily solved by simple LU decomposition without deteriorating the speed or accuracy of the scheme.

3.2 Filtering

Usually DG schemes using central flux with sufficient resolutions are accurate and stable for linear problems. However, due to the vastly separate scales in this problem with very small domains or some domains with high material coefficients, we observe that the use of a weak exponential filter can be beneficial at moderate resolution points to improve the stability. The detailed discussion on this filtering of spectral method is shown earlier by Hesthaven and Kirby [4]. Here, we briefly present the formulation of a weak exponential filter used in our scheme.

Let $\mathcal{F}_N$ be the filter operator for the polynomial of order N. Then, it can be written as

$$\mathcal{F}_Nq^k(x,t)=\sum_{i=0}^{N}\sigma_E\left(\frac{i}{N}\right)\hat{q}_i^k(t)P_i(x),$$

where

$$\sigma_E(\eta)=\exp(-\alpha\eta^p),\ \ \alpha=-\ln(\varepsilon_M),\ \ \varepsilon_M=\text{machine precision},\ \ p\geq 16.$$

Now we define the following matrix.

$$\begin{aligned}
&\mathbf{V}_{ij}=P_j(x_i),\quad 0\leq i,j\leq N\\
&\mathbf{F}=[\mathcal{F}_{ii}]=\left[\sigma_E\left(\frac{i}{N}\right)\right],\quad 0\leq i\leq N,
\end{aligned}$$

where x_i is the Legendre-Gauss-Lobatto quadrature point. Then, by substitution, we obtain

$$\mathcal{F}_N \mathbf{q}_N^k = \mathbf{VF}\ \hat{\mathbf{q}}_N^k = \mathbf{VFV}^{-1}\ \mathbf{q}_N^k,$$

where $\mathbf{q}_N^k = [q_0^k, \cdots, q_N^k]^T$ and $\hat{\mathbf{q}}_N^k = [\hat{q}_0^k, \cdots, \hat{q}_N^k]^T$.

3.3 Absorbing boundary conditions

To attenuate the scattering waves at outer boundaries, we use an absorbing boundary condition (ABC) at each end of the whole domain to suppress reflections of the waves to an acceptable level. This permits the solution to remain valid even for long time intervals [15]. The ABC is to introduce a simple sponge layer with loss in both the magnetic and electromagnetic tensors such as,

$$\nabla \times \mathbf{H}(r) = -i\frac{\omega}{c}\hat{\varepsilon}(z)\begin{bmatrix} s_z & 0 \\ 0 & s_z \end{bmatrix}\mathbf{E}(r).$$

Substituting $s_z = 1 + \frac{c\sigma_z}{i\omega}\hat{\varepsilon}^{-1}(z)$, we have

$$\nabla \times \mathbf{H}(r) = -i\frac{\omega}{c}\hat{\varepsilon}(z)\mathbf{E}(r) + \sigma_z \mathbf{E}(r),$$

where $\sigma_z(z) = (z/d)^m \sigma_{max}$, $m = 2, 3, 4$, $\sigma_{max} = 1/\Delta t$.

3.4 Numerical tests

To verify the convergence and the accuracy of the scheme, we now discuss a couple of numerical convergence tests. The first test concerns the convergence to an analytically known solution and the second one the convergence of transmission/reflection coefficients for simple isotropic materials.

3.4.1 Convergence test: isotropic/anisotropic materials

This first test can be found in [5]. Here we extend it to a slightly more general case including anisotropic materials. Let us consider the following Maxwell's equations

$$\begin{bmatrix} \varepsilon_{xx} & \varepsilon_{xy} \\ \varepsilon_{xy} & \varepsilon_{yy} \end{bmatrix}\frac{\partial}{\partial t}\begin{bmatrix} E_x \\ E_y \end{bmatrix} = \begin{bmatrix} 0 & -1 \\ 1 & 0 \end{bmatrix}\frac{\partial}{\partial z}\begin{bmatrix} H_x \\ H_y \end{bmatrix},$$
$$\frac{\partial}{\partial t}\begin{bmatrix} H_x \\ H_y \end{bmatrix} = -\begin{bmatrix} 0 & -1 \\ 1 & 0 \end{bmatrix}\frac{\partial}{\partial z}\begin{bmatrix} E_x \\ E_y \end{bmatrix}. \tag{3.8}$$

and a one-dimensional electromagnetic resonator with perfectly conducting walls located at $z^{(1)} = -1$ and $z^{(2)} = 1$. The interior of the resonator is filled with two dielectric media

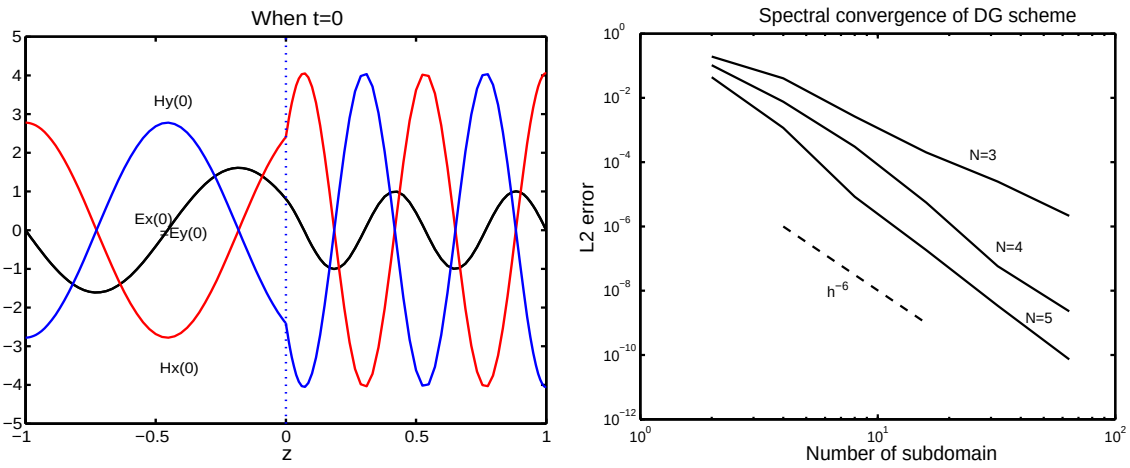

Figure 3: The solution E_x, E_y, H_x, H_y of the numerical test 1 at $t=0$ for case 2 (left) and its spectral convergence (right).

with the material interface at z=0. We impose the following boundary conditions at $z=\pm 1$ and $z=0$

$$\text{i)}\ \ \mathbf{E}=0 \ \ \text{or} \ \ \frac{\partial \mathbf{H}}{\partial z}=0, \quad \text{at} \ \ z=\pm 1,$$
$$\text{ii)}\ \ \mathbf{E}^{(1)}=\mathbf{E}^{(2)}, \quad \mathbf{H}^{(1)}=\mathbf{H}^{(2)}, \quad \text{at} \ \ z=\pm 0.$$

The solution of Maxwell's equations (3.8) satisfying the above boundary conditions can be expressed as

$$\begin{aligned}
E_x &= [A^{(k)}e^{in^{(k)}\omega z}-B^{(k)}e^{-in^{(k)}\omega z}],\\
E_y &= [A^{(k)}e^{in^{(k)}\omega z}-B^{(k)}e^{-in^{(k)}\omega z}],\\
H_x &= n^{(k)}[A^{(k)}e^{in^{(k)}\omega z}+B^{(k)}e^{-in^{(k)}\omega z}],\\
H_y &= -n^{(k)}[A^{(k)}e^{in^{(k)}\omega z}+B^{(k)}e^{-in^{(k)}\omega z}],
\end{aligned}$$

where

$$\begin{aligned}
&A^{(1)}=\frac{n^{(2)}\cos(n^{(2)}\omega)}{n^{(1)}\cos(n^{(1)}\omega)}, \quad A^{(2)}=e^{-i\omega(n^{(1)}+n^{(2)})},\\
&B^{(1)}=A^{(1)}e^{-i2n^{(1)}\omega}, \quad B^{(2)}=A^{(2)}e^{i2n^{(2)}\omega},\\
&n^{(k)}=\sqrt{\varepsilon_{xx}^{(k)}+\varepsilon_{xy}^{(k)}}=\sqrt{\varepsilon_{yy}^{(k)}+\varepsilon_{xy}^{(k)}}, \quad \text{where} \ \ \varepsilon_{xx}^{(k)}=\varepsilon_{yy}^{(k)} \ \text{is required.}
\end{aligned}$$

Here $n^{(k)}=\sqrt{\varepsilon^{(k)}}$ is the index of refraction in k^{th} material and ω is the solution of the equation

$$-n^{(2)}\tan(n^{(1)}\omega)=n^{(1)}\tan(n^{(2)}\omega),$$

and we consider the following two cases.

$$\begin{aligned}
\text{Case 1} \quad &: \quad \varepsilon_{xx}=\varepsilon_{yy}=1.0, \quad \varepsilon_{xy}=0, \qquad -1\le z\le 0,\\
&\qquad\quad \varepsilon_{xx}=\varepsilon_{yy}=2.25, \quad \varepsilon_{xy}=0, \qquad 0\le z\le 1,\\
\text{Case 2} \quad &: \quad \varepsilon_{xx}=\varepsilon_{yy}=1.0, \quad \varepsilon_{xy}=0, \qquad -1\le z\le 0,\\
&\qquad\quad \varepsilon_{xx}=\varepsilon_{yy}=4.0, \quad \varepsilon_{xy}=1.5, \qquad 0\le z\le 1.
\end{aligned}$$

Using a very small time step, we show the spectral convergence as in the right in Fig. 3. Also, with $\Delta t=\text{CFL}*(2/N)$, $\text{CFL}<1$, we can see the third order temporal convergence of the scheme in the following two tables:

1. N is the number of grid points

	N=8	N=16	N=32	N=64	N=128
L_2Error	2.1088e-002	2.8870e-003	3.7544e-004	4.7073e-005	5.9164e-006
Ratio	-	7.3045	7.6896	7.9757	7.9564
Order	-	2.8688	2.9429	2.9956	2.9921

2. N is the number of grid points

	N=8	N=16	N=32	N=64	N=128
L_2Error	3.9821e-001	4.3088e-003	6.3444e-004	7.8858e-005	1.0164e-005
Ratio	-	92.4178	6.7915	8.0453	7.7586
Order	-	6.5301	2.7637	3.0082	2.9558

3.4.2 Transmission test

Given the seminal importance of correct transmission and reflection behavior at material interfaces, it is important to confirm this behaviour correctly. Moreover, it is also of significance in DG schemes, since the behavior of electromagnetic waves on the interfaces is mainly dealt through the flux terms in DG schemes. In other words, if the transmission rate or the reflection rate does not converge to the known value, it is very likely to reflect an improper use of the flux and violation of necessary boundary conditions ($n_1\cdot\varepsilon_1 E_1=n_2\cdot\varepsilon_2 E_2$, $n\times H_1=n\times H_2$) on the interfaces. Let us consider the following Maxwell's equations

$$\begin{bmatrix} n^2 & 0\\ 0 & n^2 \end{bmatrix}\frac{\partial}{\partial t}\begin{bmatrix} E_x\\ E_y \end{bmatrix}=\begin{bmatrix} 0 & -1\\ 1 & 0 \end{bmatrix}\frac{\partial}{\partial z}\begin{bmatrix} H_x\\ H_y \end{bmatrix},$$
$$\frac{\partial}{\partial t}\begin{bmatrix} H_x\\ H_y \end{bmatrix}=-\begin{bmatrix} 0 & -1\\ 1 & 0 \end{bmatrix}\frac{\partial}{\partial z}\begin{bmatrix} E_x\\ E_y \end{bmatrix}.$$

The following results confirm the convergence of transmission/reflection rates

1. When $n_1=1.0, n_2=1.5$

	N=6	N=12
Exact value(T/R)	0.96 / 0.04	0.96 / 0.04
By computation(T/R)	0.9593 / 0.0398	0.9599 / 0.04

2. When $n_1=1.5, n_2=1.0$

	N=6	N=12
Exact value(T/R)	0.8889 / 0.1111	0.8889 / 0.1111
By computation(T/R)	0.8908 / 0.1092	0.8888 / 0.1112

4 Modeling of the frozen mode

In the following, we discuss a number of computational studies to confirm the predicted behavior and the appearance of the frozen mode. We focus on a direct validation of the theory as well as an attempt to understand the limitations of the phenomenon in crystals of finite extent.

4.1 Modeling with a large number of unit cells

In this section, we model two different types of the frozen modes with as large number of unit cells as possible to observe distinctive features of the phenomena. 200 unit cells for gyrotropic photonic crystals and 100 unit cells for oblique anisotropic layers are used in each modelings. This can be viewed an an attempt to directly validate the theories as laid out in [18–20].

4.1.1 The magnetic frozen mode

The infinite gyrotropic material is modeled with 200 unit cells of the type as shown in Fig. 2. As soon as the electromagnetic plane wave enters the slab, the wave gets amplified, it slows down and the field amplitude ($|\Psi|^2=|E_x^2+E_y^2+H_x^2+H_y^2|^2$) increases dramatically inside the slab as shown in Figs. 4 and 5. If we consider the maximum peak of the field amplitude as the forefront of the energy density, the average group velocity of the wave, which approximately coincides with the velocity of energy density transfer [17], is around 0.0015c and the average signal velocity, which is defined from the position of half-maximum intensity of the wave [17], is around 0.01c, with c being the speed of light in vacuum. Also, from the right of Fig. 5, we observe that the maximum height of field amplitude increases almost linearly and is proportional to the amount of the transmitted wave into the layer. This is in accordance with the predictions [18–20].

Generally, the energy density flux can be expressed as $<S>=<u>\cdot v$, where $<u>$ is the energy density and v is the group velocity. While the energy density flux remains

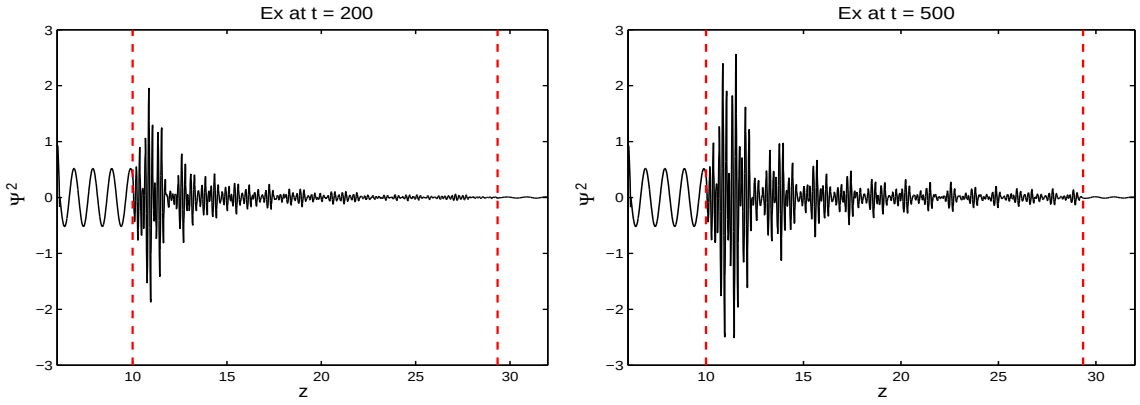

Figure 4: Electric field at the frozen mode frequency. Ncell: Number of unit cell$=200$, N: Number of grid points per each cell$=8$. $\Delta t=0.02$. $T=200$ (left), $T=500$ (right). The incident field is E$\|$x polarized. The dotted lines indicate the outer boundaries of the crystal.

approximately constant, the energy density inside the slab grows enormously in proportion to the amount of the transmitted wave. The group velocity is inversely proportional to the energy density, so the wave gets slowed down accordingly (Fig. 6).

Also note that energy density flux is almost the same for these two materials, but the energy density in the magnetic material is much higher than that in anisotropic material. Consequently, the group velocity of the wave is much slower in the magnetic materials. This is why we see two lines in group velocity and energy density in Fig. 6.

If an electromagnetic wave at the frozen mode frequency propagates in the opposite direction, we clearly see that abnormality of the frozen mode has disappeared (left in Fig. 7). The electromagnetic wave reaches the other end with normal speed and there is no amplification of the field amplitude. Similarly, if the thickness ratio of **F** or the frequency of the incident wave is changed a little bit, none of the distinctive features of the frozen mode is observed, as also illustrated in Fig. 7.

4.1.2 The oblique frozen mode

We repeat the computational experiment for the purely dielectric case using 100 unit cells of the type shown in Fig. 2. We display the electromagnetic wave in Fig. 8 and the field amplitude in Fig. 9 inside the oblique anisotropic layers along the z-direction.

The features of the oblique frozen mode are similar to those of the magnetic frozen mode, although the shape of the wave and value of the field amplitude are quite different. At T=500.0, the highest amplification of the field amplitude is around 5.9 which is much smaller than that of the magnetic frozen mode where it was exceeding 90. The average group velocity inside the layer is approximately 0.03c, which is significantly faster than the magnetic case (0.0015c). Different from the magnetic frozen mode, the average signal velocity is 0.03c, which is the same as the average group velocity for the oblique frozen mode.

The energy density flux is similar to that of the magnetic froze mode. However, since

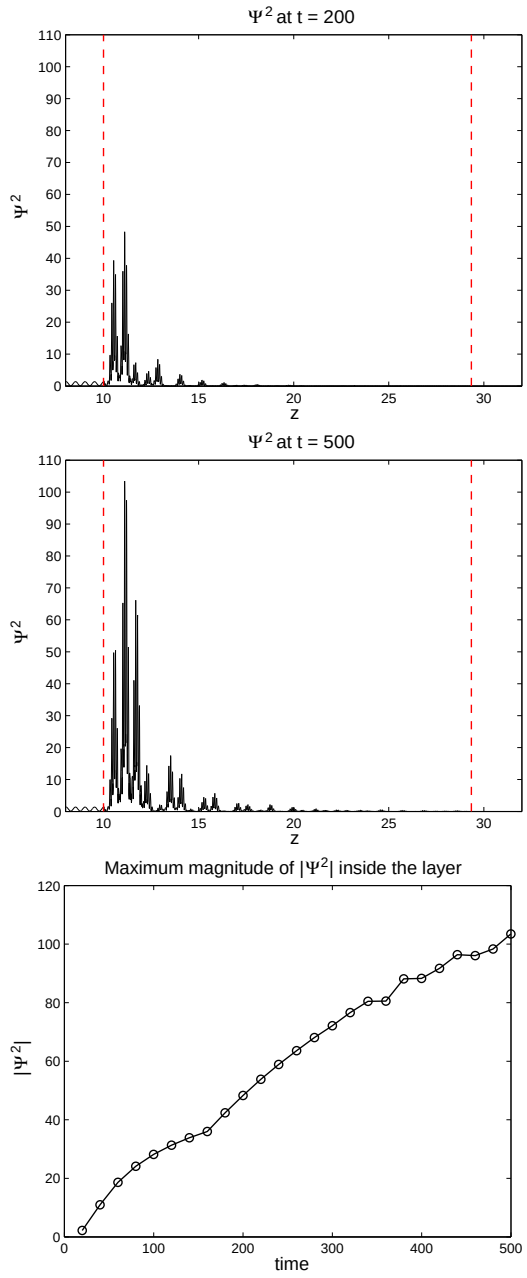

Figure 5: Field amplitude ($|\psi|^2$) at the frozen mode frequency. Ncell=200, N=8. T=200 (top), T=500 (middle). The bottom graph shows that the maximum magnitude of field amplitude increases linearly with time. The incident field is E$\|$x polarized. The dotted lines indicate the outer boundaries of the crystal.

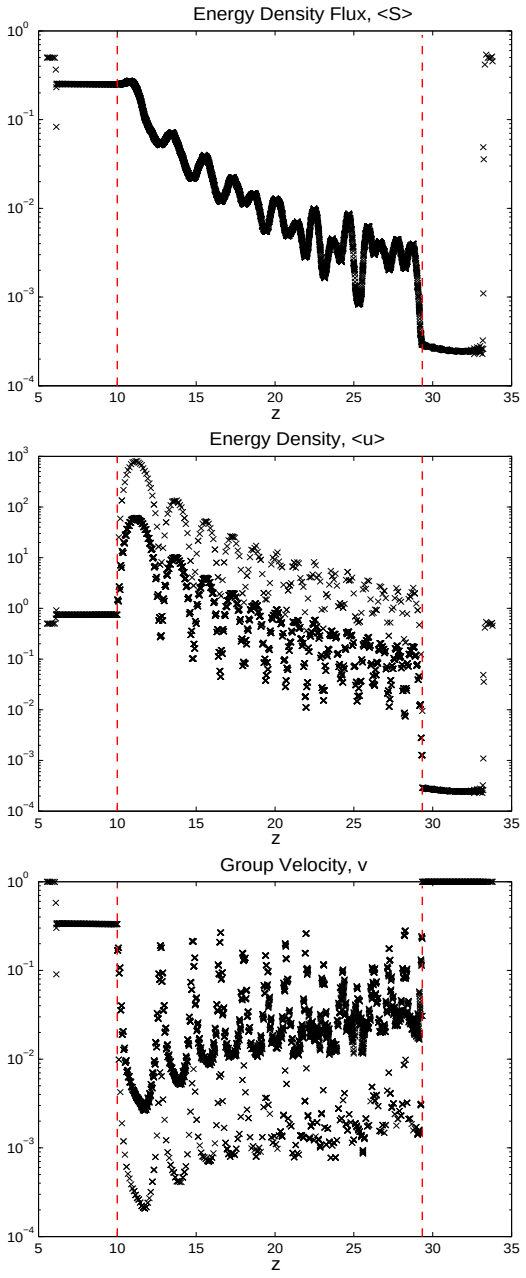

Figure 6: Energy density flux (top), Energy density (middle), group velocity (bottom) at the frozen mode frequency in the gyrotropic photonic crystals when $T = 500$. Energy density is different between magnetic material and anisotropic material, so this is why we see two separate lines of groups in energy density and group velocity. The incident wave is with constant amplitude and E$\|$x polarized. The dotted line indicates the outer boundaries of the crystal.

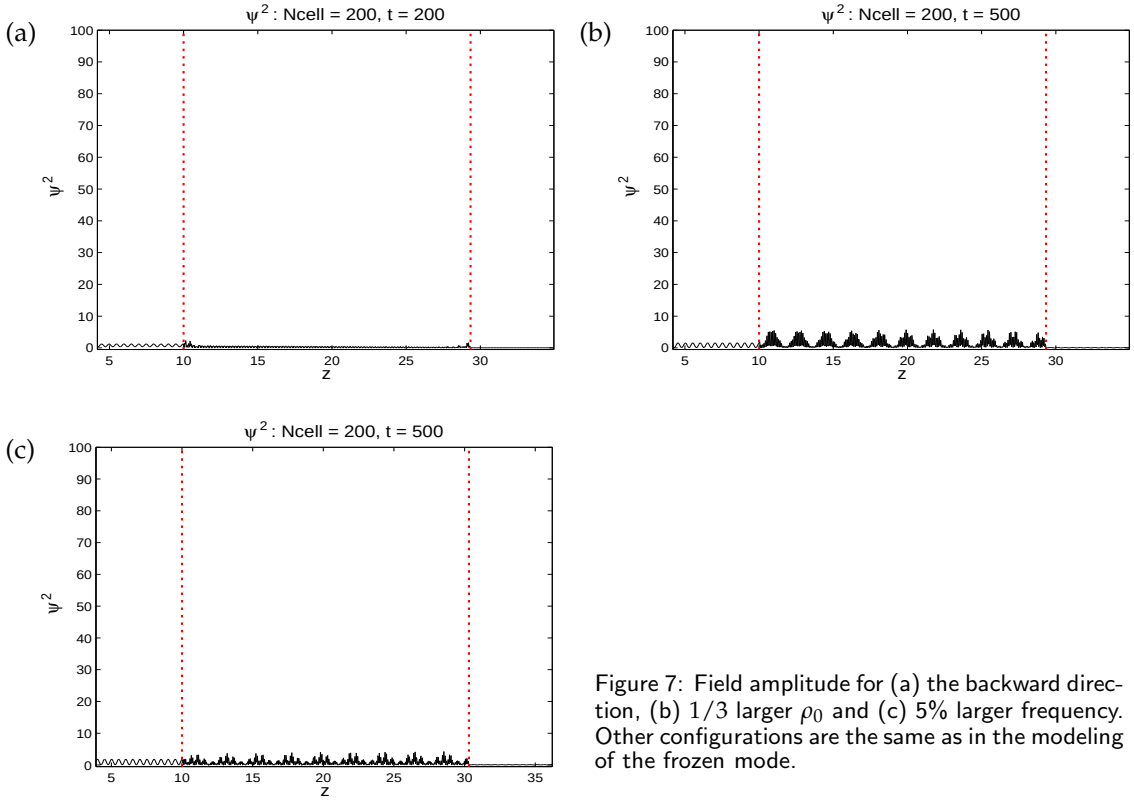

Figure 7: Field amplitude for (a) the backward direction, (b) $1/3$ larger ρ_0 and (c) 5% larger frequency. Other configurations are the same as in the modeling of the frozen mode.

the larger energy density flux leaves the layer, the energy density is much smaller, e.g., the energy density flux out of the last cell of gyrotropic photonic crystal is around 10^{-3}, but that of oblique anisotropic layer is around 10^{-2}, 10 times larger. Thus, the group velocity of the wave is much faster than that of the wave in the gyrotropic photonic crystals. Similar to the magnetic crystal, changes in direction of propagation or frequency dramatically alter the behavior of the frozen mode as illustrated in Fig. 11.

4.2 Modeling with small number of unit cells

The existence of the frozen mode is theoretically based on the assumption that the layer is semi-infinite, but less is known about the phenomena for crystals with a finite small number of unit cells. In this section, we first determine the smallest number of unit cells required for the frozen mode, then study how the finiteness of layer changes the features of the frozen mode.

4.2.1 Compressibility condition

If we take a careful look at the phenomena, we note that the phenomena can be characterized by the compressibility of the electromagnetic waves. In other words, the energy

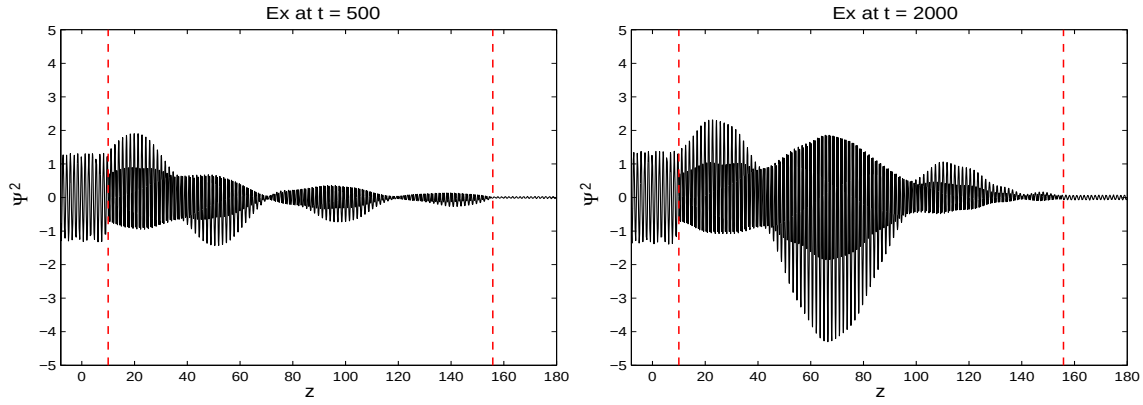

Figure 8: Electric field along the x-direction of the oblique frozen mode at $T=500$ (left), $T=2000$ (right). N: Number of grid points per each cell $=16$. $\Delta t=0.02$, Number of cell$=100$. TM polarization. The dotted lines indicate the outer boundaries of the layer.

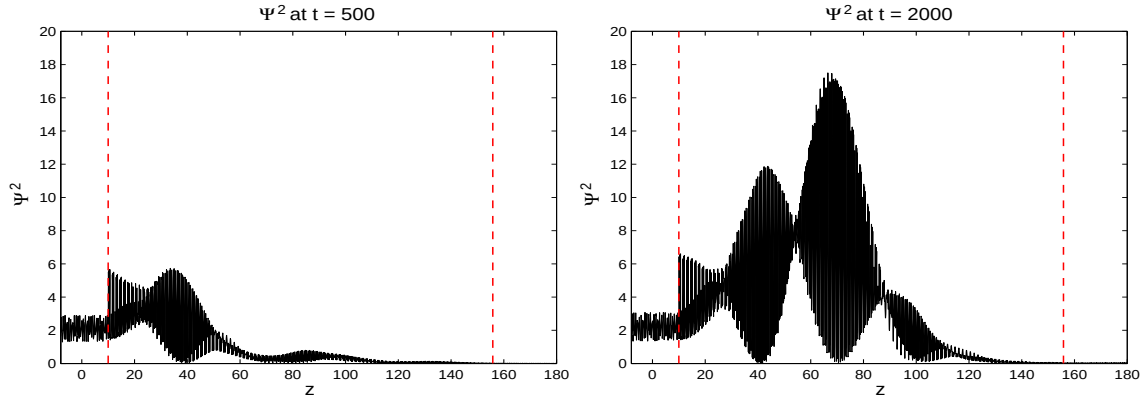

Figure 9: Field amplitude $|\Psi|^2$ of the oblique frozen mode at $T=500$ (left), $T=2000$ (right). $N=16$, Number of cell$=100$. TM polarization. The dotted lines indicate the outer boundaries of the slab.

density flux ($\mathbf{e}_f$) should satisfy the following compressibility condition for the occurrence of the frozen mode

$$\int_S \mathbf{e}_f \cdot n ds = \int_V \nabla \mathbf{e}_f dV > 0.$$

If the above integral is zero, no energy density stacks up inside the layer as what enters the crystal also leaves it. However, if the integral is positive, the amount of the influx wave is larger than that of outflow wave and consequently energy stacks up inside the layer and gets compressed, reflecting a slow-down of the wave and sharp increase of the field amplitude. This compressibility condition is thus a measure of the energy density flux for the frozen mode. If a layer is finite, the compressibility condition holds only for a finite time T_c, but it is significantly longer than time T_0 when a wave propagates and reaches the same distance in the similar material without showing the frozen mode.

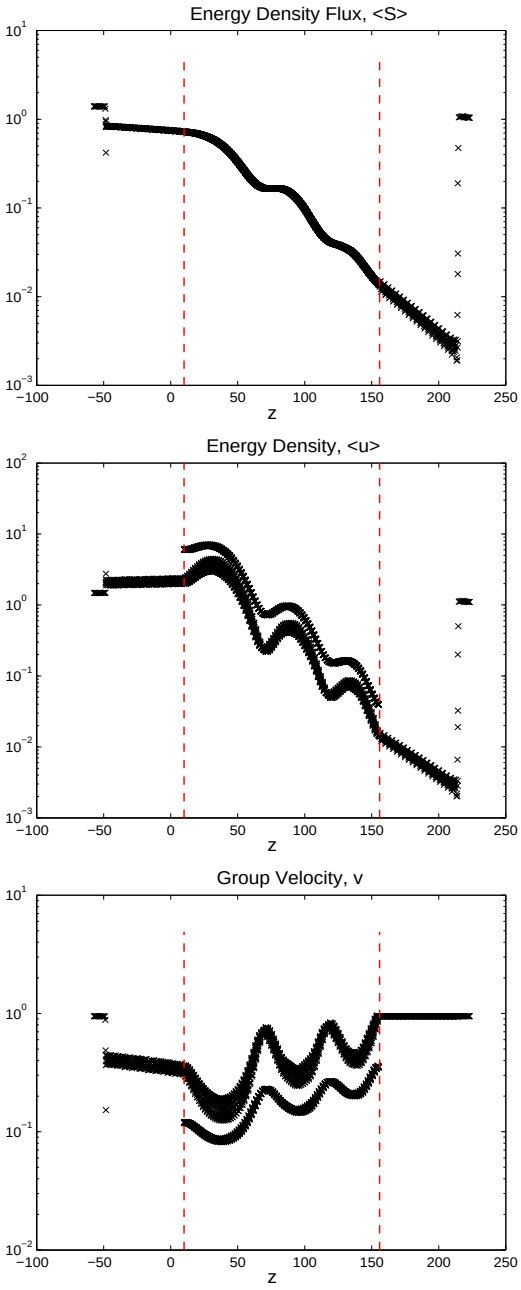

Figure 10: Energy density flux (top), Energy density (middle), group velocity (bottom) at the frozen mode frequency in the oblique crystal. $T = 2000$. The energy density is higher in anisotropic material than in vacuum. T=500. TM polarization. The dotted lines indicate the outer boundaries of the layer.

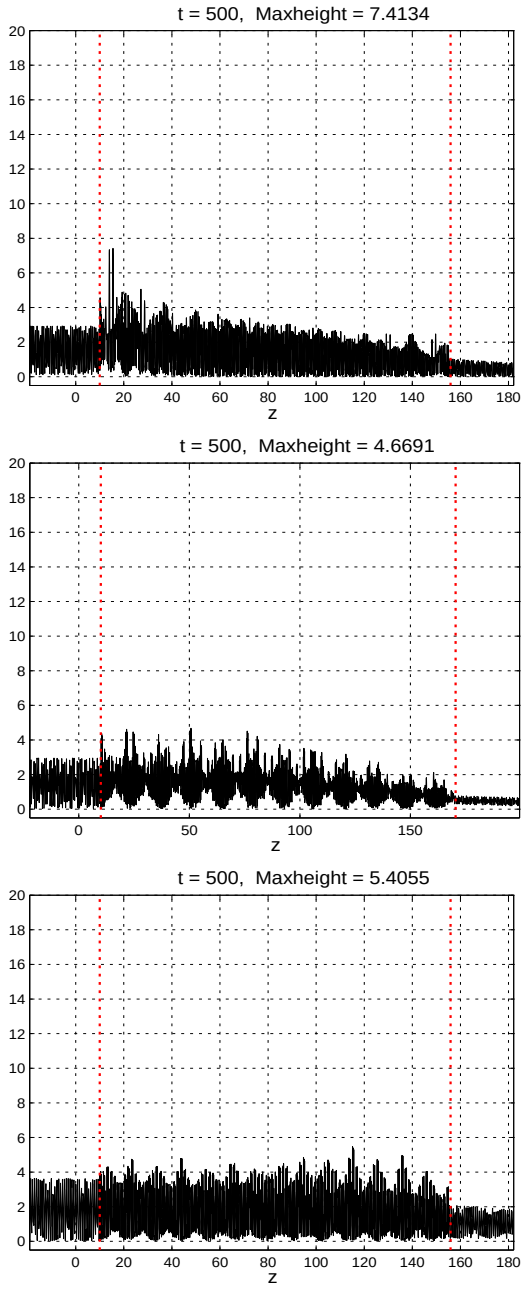

Figure 11: Field amplitude $|\Psi|^2$ at $T = 500$ when the direction of the wave is backward (top), the frequency is 10% larger (middle) than the center frequency, and the angle of incidence is 10% larger (bottom). $N = 16$. TM polarization. The dotted lines indicate the outer boundaries of the layer.

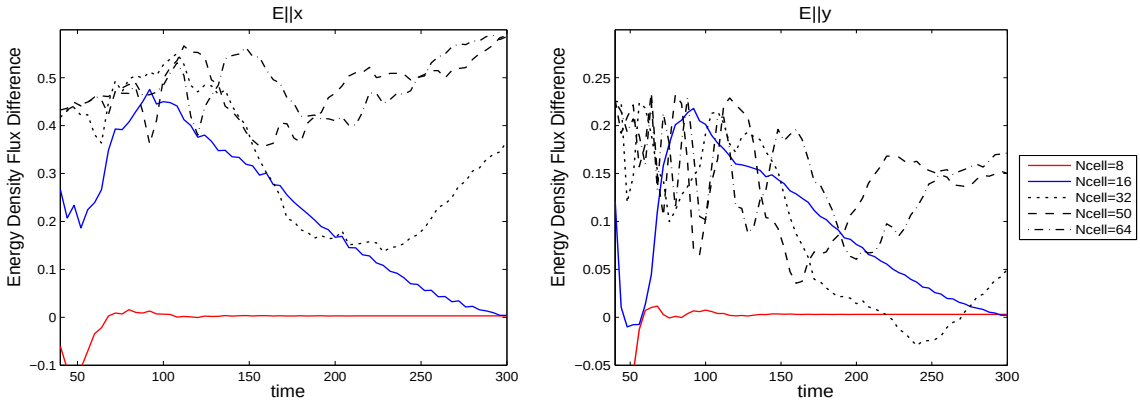

Figure 12: The magnetic frozen mode for $E||x$ polarization (left), $E||y$ polarization (right): EDFD vs. number of cells (Ncell). Ncell=8 (solid low flat line), Ncell=16 (decreasing solid line), Ncell=32 (dotted line), Ncell=50 (dashed line), Ncell=64 (dotted-dashed lines). $T=300$.

In a one-dimensional finite case, we have only two fluxes, inflow and outflow in z direction. Thus, the compressibility condition can be simply expressed as

$$e_f|_{z_{in}} - e_f|_{z_{out}} > 0, \qquad \text{while} \quad t < T_c, \quad T_c \gg T_0.$$

If we refer to the left quantity as *Energy Density Flux difference (EDFD)*, it is clear that as this EDFD gets larger, this reflects more distinctive features of the frozen mode inside the layer.

4.2.2 How many cells are needed for the phenomena?

Fig. 12 shows EDFD of the magnetic frozen mode for various numbers of unit cells. With 8 unit cells, we hardly see any significant values of EDFD, reflecting an inability to sustain the frozen mode. However, with only 16 unit cells, the EDFD reaches around 0.5 and linearly decreases to zero up to T=300.0. For 32, 50, or 64 unit cells, we observe a relatively high EDFD, although all eventually approaches to zero after a long time integration. Thus, it appears that approximately 16 unit cells are sufficient for the magnetic frozen mode. The field amplitude, energy density flux, and group velocity with 16 unit cells at T=150 are shown in Fig. 13 where we recognize the characteristics of the phenomena, although the intensity is rather small.

In Fig. 14, we show the field amplitude, energy density flux, and group velocity with 32 unit cells in the oblique anisotropic layers at T=150. Also, EDFDs for various numbers of unit cells are shown in Fig. 15. We notice that at least 32 cells are required for a distinctive frozen mode, i.e., twice as many as the number of the magnetic frozen mode.

4.2.3 Transmittance rate

Even with a small number of unit cells, we observe that there are still amplifications of the field amplitude and slow-down of waves. What happens, however, with the transmittance rate?

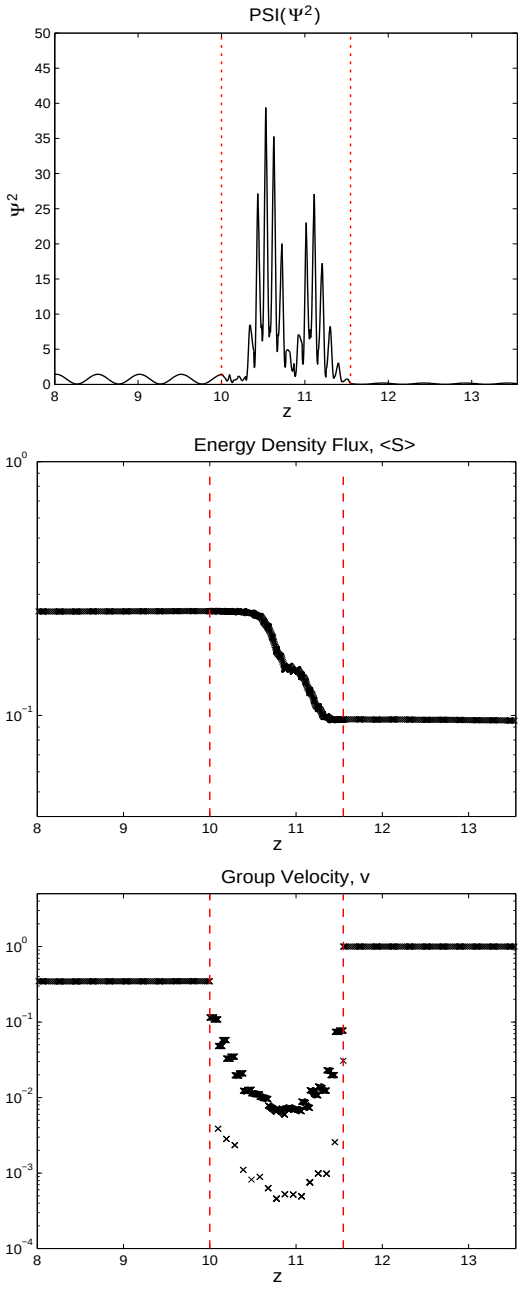

Figure 13: The magnetic frozen mode with 16 unit cells: Field amplitude $|\Psi|^2$ (top), energy density flux (middle), and group velocity (bottom) at $T=150$. The incident wave is $E \| x$ polarized.

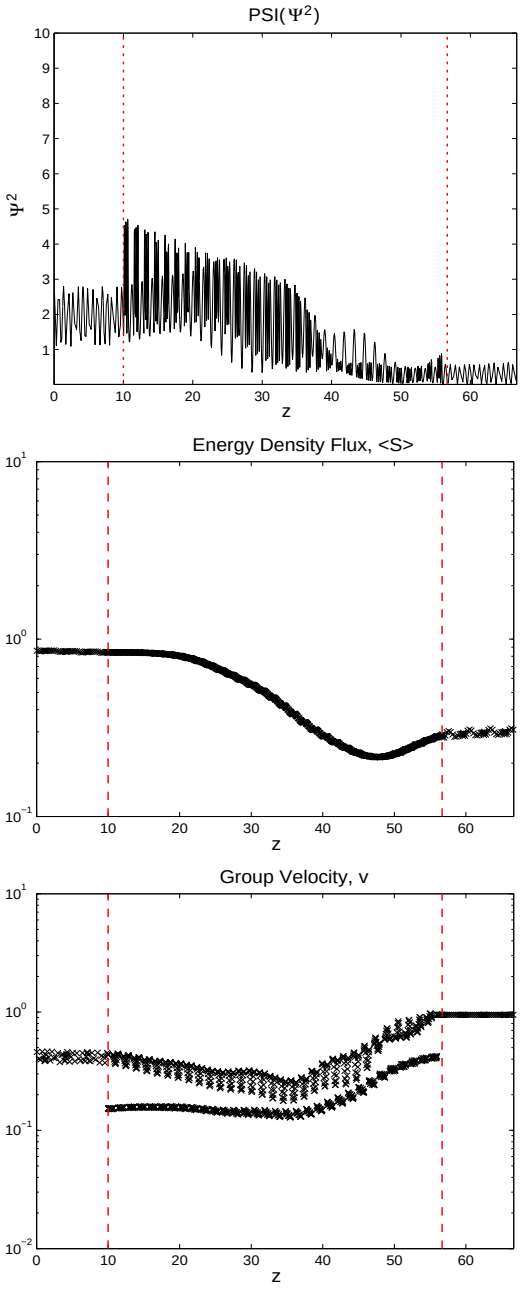

Figure 14: The oblique frozen mode with 32 unit cells: Field amplitude $|\Psi|^2$ (top), Energy density (middle), and group velocity (bottom) at $T=150$. The incident wave is TM polarized.

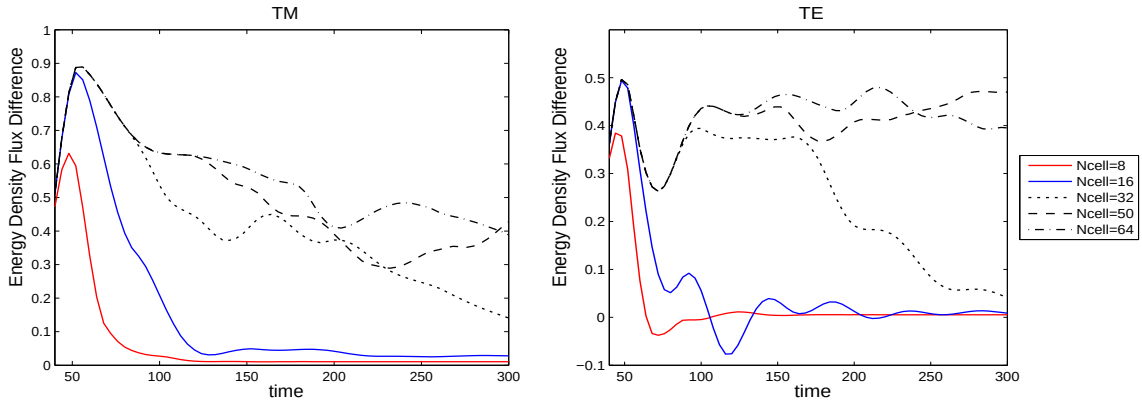

Figure 15: The oblique frozen mode for each polarizations at $T=300$. TM polarization (left), TE polarization (right): Ncell$=8$ (lowest solid line), Ncell$=16$ (second lowest solid line), Ncell$=32$ (dotted line), Ncell$=50$ (dashed line), Ncell$=64$ (dotted-dashed lines).

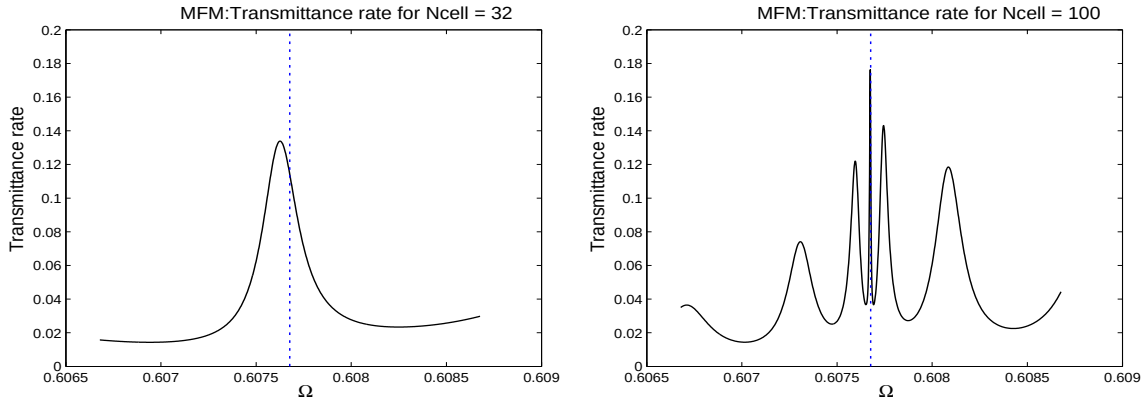

Figure 16: Predicted transmittance rate for a finite number of cells$=32$ (left), 100 (right). The dotted line denotes the frozen mode frequency. The difference between the frozen mode frequency and the peak is 5×10^{-5} for 32 unit cells, 1×2^{-6} for 100 unit cells.

In the paper [19], it is shown that the transmittance rate displays its cup-like singularity at the frozen mode frequency ω_0 when the layer is infinite. On the other hand, when the layer consists of finite number of unit cells, the singularity shifts a little bit from ω_0, but as the number of unit cells increases, the singularity approaches to ω_0 as shown in Fig. 16.

Fig. 17 shows the computed values of the transmittance rate in the time domain for two different polarization $E||x$ and $E||y$ of the magnetic crystal with 16 unit cells. As predicted, there are shifts of the peak of the transmittance rate curve by the difference of 0.0912 and 0.0304 for $E||x$, $E||y$ respectively. However, we also observe highly oscillatory transmittance rates for both polarizations due to the finiteness of the slab and recognize them as the Fabry-Pérot peaks.

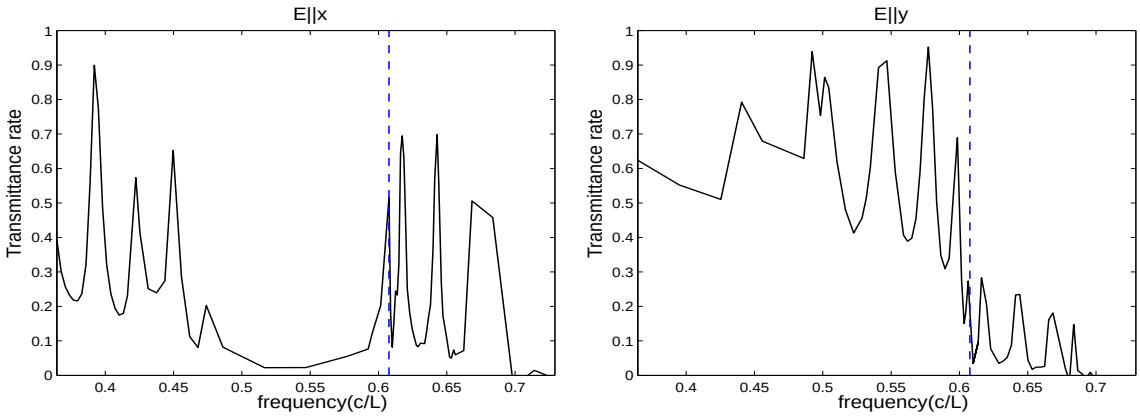

Figure 17: Computed values of the transmittance rate for the magnetic frozen mode with 16 unit cells for each polarization E||x (left), E||y (right). The lowest peak for E||x is at 0.6988 with 0.0912 difference and the highest peak for E||y is at 0.5773 with 0.0304 difference.

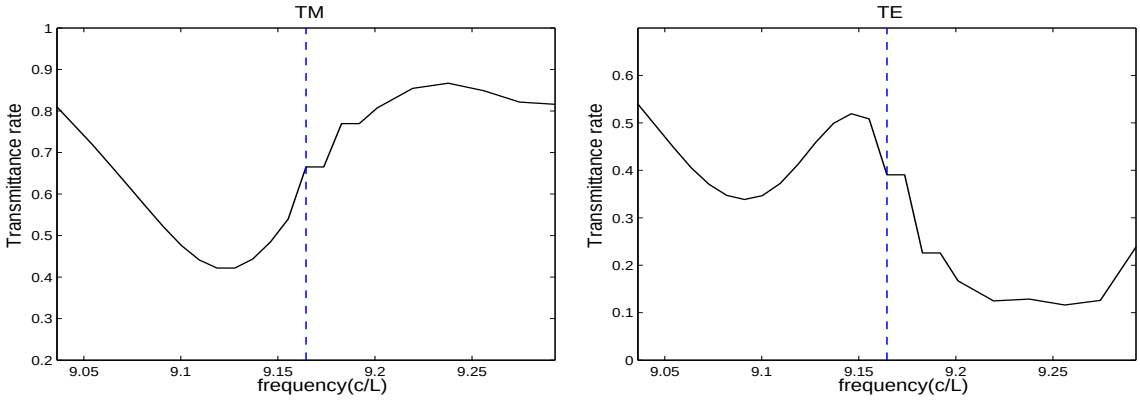

Figure 18: Computed values of transmittance rate for the oblique frozen mode with 32 unit cells for each polarization TM (left), TE (right). The lowest peak of TM polarization is at 9.1186 with 0.0458 difference and the highest peak of TE polarization is at 9.1278 with 0.0367 difference.

For the oblique frozen mode with 32 unit cells, there are also shifts of the peak by 0.0458, 0.0367 for TM and TE polarization, as illustrated in Fig. 18, but no Fabry-Pérot peaks are observed.

5 Sensitivity of frozen mode

As we have seen in the previous section, the frozen mode phenomenon, predicted under ideal and impractical assumptions, appears to also exist under more realistic conditions such as finite length crystals. However, the results also emphasize that changes in the various parameters such as frequency or layer length could destroy the phenomenon. In fact, the material properties of layers (thickness of each layer, misalignment angle for

anisotropic layer, material constants) and characteristics of wave propagation(incident angle, frequency) should be exact up to 3∼4 digits to generate a stationary inflection point obtained by analytic methods. However, even with current state-of-the-art technology, it seems to be very hard to meet such standards. Thus, it is very likely one faces some errors in the fabrication of the crystal layers and in propagating an electromagnetic wave with the exact frequency.

In this section, we study how such errors in the parameters of the layers or illuminating wave will impact the frozen mode with the goal of providing guidelines on how much error is allowable without destroying the frozen mode. For this purpose, we perform two different tests: One is to observe EDFD for the same amount of errors in each parameters and the other is to observe the independently randomized errors on each parameters within a certain range. The former represents a systematic error while the latter reflects randomized errors during fabrication or operation. The thickness of the magnetic layer **F** and the misalignment of the anisotropic **A** layers are considered in the magnetic frozen mode, while the thickness of the anisotropic **A** layer and the incident angle of the wave are used for the oblique frozen mode, see Fig. 2.

5.1 Correlated uncertainty

In Fig. 19, we show EDFD for variations in the thickness of **F** layer or different misalignment angle of **A** layer for each polarization E$\|$x (left) and E$\|$y (right). We observe that the maximum of EDFD is shifted from 100 % to a value around 98%∼99% of the frozen mode frequency due to the finiteness of the layer. If we set 25% of the maximum of EDFD as the limit of EDFD for the frozen mode, then an allowable error is [95.5, 101.0] for the thickness of the **F** layer and [96.5, 100.5] for the misalignment angle. This analysis indicates that the misalignment angle of **A** layer is a little more sensitive than the thickness of **F** layer.

For the oblique frozen mode, EDFD for TE polarization is similar to that of the magnetic frozen mode, but EDFD for TM seems to be unexpected as shown in Fig. 20. As mentioned in the previous section, the energy density in the oblique anisotropic layer is not sufficiently large since the energy density flux leaving out of the slab remains significant even at the frozen mode frequency. For TE polarization, as the frequency of the incident wave approaches to the frozen mode frequency, the transmittance rate increases and the energy density flux leaving out of the layer decreases. Consequently, EDFD increases as we see on the right of Fig. 20. On the other hand, for TM polarization, as we approach to the frozen mode, the energy flux leaving out of the layer decreases, but the transmittance rate also decreases. Thus, EDFD doesn't drop sharply even though it is not in the frozen mode. However, it is still true that energy flux density leaving out of the layer is the smallest at the frozen mode frequency for both polarizations. For this reason, let's only consider TE polarization for the analysis.

Similar to the magnetic frozen mode, there are shifts of the maximum of the EDFD and the allowable error with the same cutoff as for the magnetic frozen mode is [99.0,

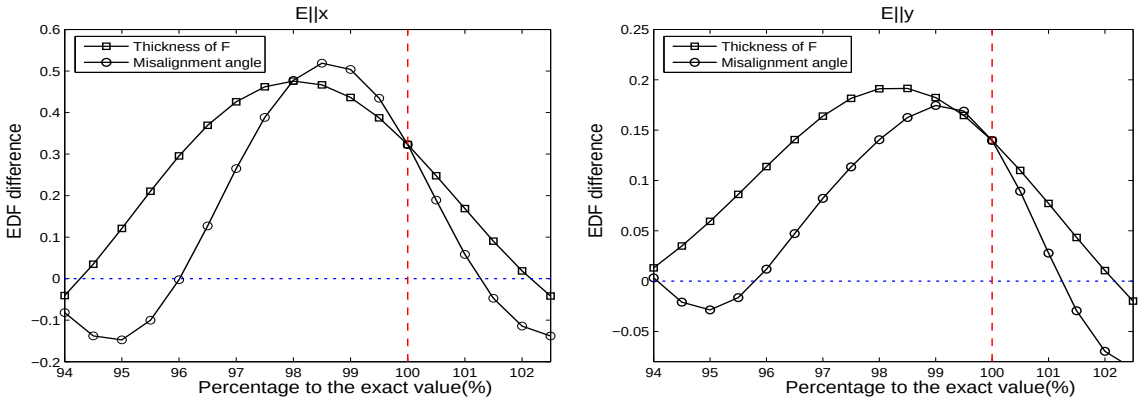

Figure 19: EDFD of the magnetic frozen mode for the thickness of **F** layer (square) and the misalignment of **A** layer (circle). The vertical line is the percentage value of parameters for the frozen mode. E$\|$x (left), E$\|$y (right). $T=150$.

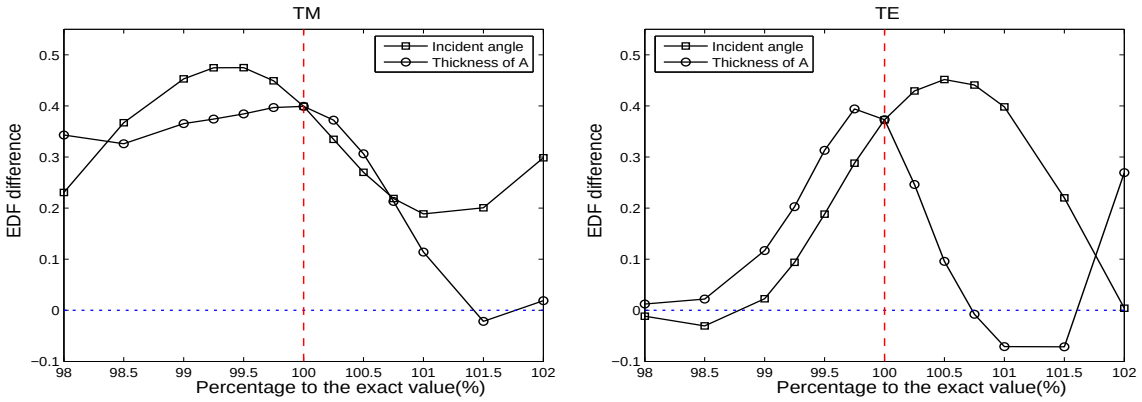

Figure 20: EDFD of the oblique frozen mode for the incident angle of the wave (square) and the thickness of **A** layer (circle) at $T=150$. The horizontal line is the percentage value of parameters for the frozen mode and the dotted vertical line is the exact frozen frequency. TM (left), TE (right).

100.5] for the incident angle of the wave and [99.5, 101.5] for the thickness of **A** layer, which is significantly smaller than that of the magnetic frozen mode which appears as a much more robust phenomenon.

5.2 Uncorrelated uncertainty

In this section, we assume that each parameter in the crystal can vary independently and has own i.i.d. random variable within a given uncertainty associated, which implies we shall study the expectation and what amount of uncertainty will be sufficient to destroy the frozen mode.

First, we let the parameter be the incident angle of the wave. We have one input (incident angle) and one output (EDFD). Using Gauss quadrature, we obtain the expectation

as follows:

$$\bar{\mathbf{E}}(n)=\int \mathrm{EDFD}(n,z)\rho(z)dz=\sum_{k=1}^{M}\mathrm{EDFD}(n,z_k)\omega_k,$$

assuming that the random variables are uniformly distributed. Here, z_k is the Legendre-Gauss-Lobatto point and ω_k the weight. But, for other parameters, we need different ways of estimation. Let the number of cells for the magnetic frozen mode and the oblique frozen mode be 16 and 32, respectively. Then, we have 32 input parameters for the thickness of **A** layer for the oblique frozen mode and 16 input parameters for the thickness of **F** layer and the misalignment of **A** layer for the magnetic frozen mode. Several numerical methods can be applied to these problems, such as Monte Carlo Method and Stochastic Galerkin Method, but we use Stochastic collocation method which combines the accuracy of the Stochastic Galerkin Method and easy implementation of Monte Carlo Method [8]. We use Stroud's cubature points of degree 2 as collocation points which provide high efficiency with minimal (Ncell+1) number of nodal point sets [7]. The brief procedure takes the following steps:

1. Generate i.i.d. random variables according to Stroud-2 method

$$Y_k^{2r-1}=\sqrt{\frac{2}{3}}\cos\frac{2rk\pi}{N+1},\quad Y_k^{2r}=\sqrt{\frac{2}{3}}\sin\frac{2rk\pi}{N+1},\quad r=1,2,\cdots,[N/2],$$

   where $[N/2]$ is the greatest integer not exceeding $N/2$, and if N is odd $Y_k^N=(-1)^k/\sqrt{3}$.

2. Solve for each $k=0,\cdots,$Ncell with $\{Y_k^1,\cdots,Y_k^{\mathrm{Ncell}}\}$ and obtain each EDFD.

3. Post-process the result to evaluate the expectation

$$\mathbf{E}=\frac{1}{\mathrm{Ncell}+1}\sum_{k=0}^{\mathrm{Ncell}}\mathrm{EDFD}(k).$$

For the magnetic frozen mode, Fig. 21 shows that if we allow one standard deviation of uncertainty, then approximately 5 % uncertainty in the misalignment angle of **A** layers and as much as 15 % uncertainty of thickness of **F** layer are allowable without the EDFD being reduced below 25 % maximum value. These numbers are $2\sim5$ times larger than those for the correlated uncertainty, reflecting significant robustness of the magnetic crystal to randomized small uncertainties.

Similarly, for the oblique frozen mode, as shown in Fig. 22, the thickness of the **A** layer can vary with about 2% and the incident angle up to 5% to maintain the frozen mode characteristics within one standard deviation. Although these numbers are considerably smaller than those for the magnetic crystal, the numbers are still $2\sim10$ times larger than those found in the correlated case.

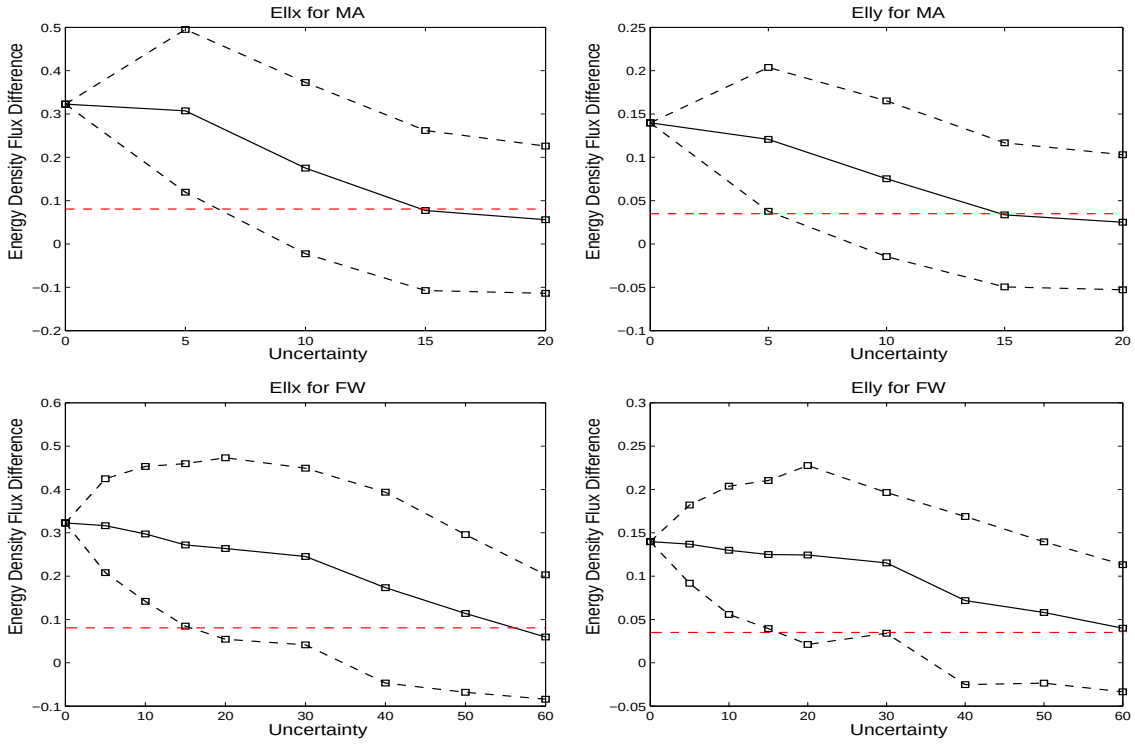

Figure 21: The magnetic frozen mode: Expectation for uncorrelated uncertainties of misalignment angle of **A** layer (MA), E$\|$x(1st)/E$\|$y(2nd) and thickness of **F** layer (FW), E$\|$x(3rd)/E$\|$y(4th). The above dotted line is E(x)$+\delta$ and the below one is E(x)$-\delta$. E(x): expectation, δ: one standard deviation. The horizontal dashed line is a cutoff amount of EDFD for the frozen mode.

6 Concluding remarks

In this work, we addressed a number of central questions regarding the recently proposed periodic structures, utilizing anisotropic materials [18–20] and expected to display a number of highly unusual and interesting phenomena such as very low propagation velocity, very high localized field intensity and also perfect transmission into crystals comprising of high-index materials.

Our first task has been to develop an accurate and efficient means, by which to model these new crystals in the time-domain with the aim of confirming the predicted behavior and further understanding the nature and limits of the theoretical predictions. We developed and validated a discontinuous Galerkin method for this purpose. As we have seen before, we are able to qualitatively and quantitatively confirm all essential predictions and further show that many of these effects can be reproduced in crystals with even moderate length.

As predicted by the theory, the finiteness of the crystal implies a slight shift in the frozen mode frequency. Furthermore, we have compared the behavior of crystals with magnetic layers as well as purely dielectric crystals with the incident wave entering at

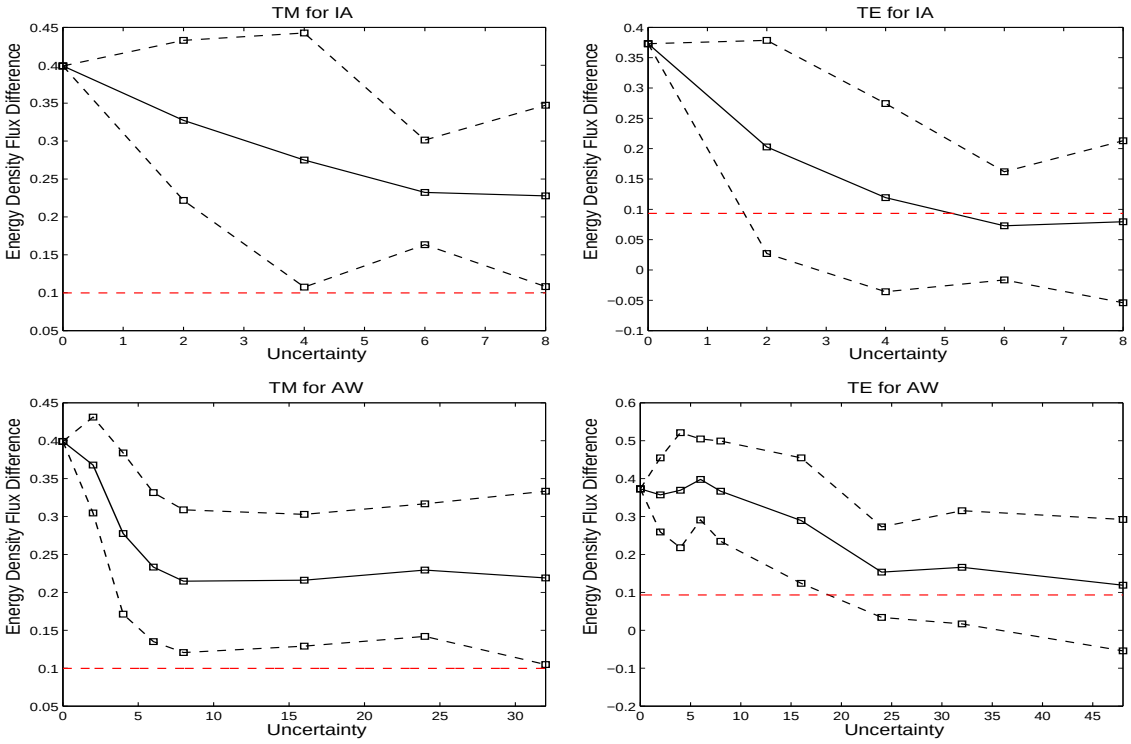

Figure 22: The oblique frozen mode: Expectation for uncorrelated uncertainties of the incident angle of the wave (IA), TM(1st)/TE(2nd) and the thickness of **A** layer (AW), TM(3rd)/TE(4th). The above dotted line is E(x)+δ and the below one is E(x)−δ. E(x): expectation, δ: standard deviation. The horizontal dashed line is a cutoff amount of EDFD for the frozen mode.

an oblique angle. While the behaviors of the two crystals are qualitatively comparable, the details are very different and the magnetic material leads to much stronger effects. Indeed, the computational results show that the amplification of the oblique frozen mode is more than 20 times lower than that of the magnetic frozen mode and the velocity of energy transfer of the oblique frozen mode is also approximately 20 times faster than that of the magnetic frozen mode. Hence, the purely dielectric crystal has to be longer to achieve similar effects. Unfortunately, even the very thin magnetic layers are problematic from a production perspective as magnetic materials with sufficient Faraday rotation and low enough loss is difficult to manufacture in the right frequency regime (microwaves).

By studying the sensitivity of the frozen mode phenomenon, we have been able to establish bounds for how large uncertainties can be without impacting the essential behavior of the crystals. These studies also confirm that the magnetic crystals are considerably more stable to variations in the crystal parameters as compared to the oblique crystal. Surprisingly, we find in both cases that systematic variations are considerably worse than uncorrelated variations in the parameters, confirming that the frozen mode phenomenon is a robust phenomenon with excellent chances of being verified experimentally, provided appropriate materials can be identified.

Acknowledgments

This work was supported by the U.S. Air Force Office of Scientific Research under the grant FA9550-04-1-0359.

References

[1] J. S. Hesthaven and T. Warburton, Discontinuous Galerkin methods for the time-domain Maxwell's equations: An introduction, ACES Newsletter, 19(1) (2004), 10-29.
[2] J. S. Hesthaven and T. Warburton, Nodal high-order methods on unstructured grids, J. Comput. Phys., 181 (2002), 186-221.
[3] J. S. Hesthaven, High-order accurate methods in time-domain computational electromagnetics: A review, Adv. Imag. Elect. Phys., 127 (2003), 59-123.
[4] J. S. Hesthaven and R. M. Kirby, Filtering in Legendre spectral methods, Math. Comput., 2007, in press.
[5] A. Ditkowski, K. Dridi and J. S. Hesthaven, Convergence cartesian grid methods for Maxwell's equations in complex geometries, J. Comput. Phys., 170 (2001), 87-101.
[6] A. H. Mohammadian, V. Shankar and W. F. Hall, Computation of electromagnetic scattering and radiation using a time-domain finite-volume discretization procedure, Comput. Phys. Commun., 68 (1991), 175-196.
[7] A. Stroud, Remarks on the disposition of points in numerical integration formulas, Math. Comput., 11 (1953), 257-261.
[8] D. Xiu and J. S. Hesthaven, High order collocation methods for differential equations with random inputs, SIAM J. Sci. Comput., 27(3) (2005), 1118-1139.
[9] U. M. Ascher and L. R. Petzold, Computer Methods for Ordinary Differential Equations and Differential-Algebraic Equations, SIAM, Philadelpha, 1998.
[10] G. Szego, Orthogonal Polynomials, Colloquium Publications, vol 23, American Mathematical Society, Providence, 1995.
[11] L. D. Landau, E. M. Lifshitz and L. P. Pitaevskii, Electrodynamics of Continuous Media, Pergamon, New York, 1984.
[12] A. Yariv and P. Yeh, Optical Waves in Crystals, Wiley Interscience, New York, 1984.
[13] A. G. Gurevich and G. A. Melkov, Magnetization Oscillations and Waves, CRC Press, New York, 1996.
[14] K. S. Kunz and R. J. Luebbers, The Finite Difference Time Domain Method for Electromagnetics, CRC Press, Florida, 1993.
[15] A. Taflove and S. C. Hagness, Computational Electrodynamics, Artech House, Boston, 2000.
[16] D. J. Griffiths, Introductions to Electrodynamics, 3rd ed., Prentice Hall, New Jersey, 1998.
[17] L. Brillouin, Wave Propagation and Group Velocity, Academic Press, New York, 1960.
[18] A. Figotin and I. Vitebsky, Nonreciprocal magnetic photonic crystals, Phys. Rev. E, 63 (2001), 0666609.
[19] A. Figotin and I. Vitebsky, Electromanetic unidirectionality in magnetic photonic crystals, Phys. Rev. B, 67 (2003), 165210.
[20] A. Figotin and I. Vitebsky, Oblique frozen modes in periodic layered media, Phys. Rev. E, 68 (2003), 036609.
[21] J. Ballato, A. Ballato, A. Figotin and I. Vitebsky, Frozen light in periodic stacks of anisotropic layers, Phys. Rev. E, 71(1) (2005), 036612.